**Title**
Identification of Blood Vessels in Cortical Bone Pores utilizing DCE-MRI and HR-pQCT



**Author**
Gibbons, Matthew

**Publication Date**
2018

Peer reviewed|Thesis/dissertation

# Identification of Blood Vessels in Cortical Bone Pores utilizing DCE-MRI and HRpQCT

by

Matthew R Gibbons

THESIS

Submitted in partial satisfaction of the requirements for the degree of

MASTER OF SCIENCE

in

Biomedical Imaging

in the

GRADUATE DIVISION

of the

UNIVERSITY OF CALIFORNIA, SAN FRANCISCO

**ACKNOWLEDGEMENTS**

I would like to thank my advisor, Dr. Galateia Kazakia, who in taking me on as a student gave me the choice of several fascinating projects. I greatly appreciate the guidance that she provided. I am grateful for the opportunity to learn have this introduction to the complexity of our skeletal system. Dr. Po Hung Wu was invaluable in getting me started with the blood vessel image analysis pipeline and giving assistance over the course of the project. Dr. Jing Liu and Dr. Roland Krug contributed advice on MRI sequences, use of contrast agents, and vetted aspects of the phantom experiments. Thanks to everyone in the Bone Quality Research Lab and Type II Diabetes project for their assistance with this work.

My thesis committee, Dr. Henry VanBrocklin, Dr. Valentina Pedoia, and Dr. Peder Larson, was very helpful with their advice during my research defense and over the course of the thesis work. Dr. Larson provided guidance on MRI artifacts and made a recommendation to do some phantom experiments for spatial calibration. Dr. Pedoia was very generous with her time giving advice on image registration algorithms and made the recommendation to perform repeatability studies.

Dr. Youngho Seo and Tony Huynh were exceptionally helpful by providing the PET phantoms for our experiments and instructions for their use. Without their assistance, an important part of this thesis would not have been completed.

I also thank Dr. Susan Noworolski for allowing me to begin this work as the project for the BI265 image analysis class, including guidance and recommendations. Moreover, a big thank you to Guillaume Trusz and Steven Su (students in the UCSF MSBI program) who were collaborators in the initial stages during the BI265 course.

This new adventure into biomedical imaging would not have been possible without the support of my wife, Elisa. We took the chance together that I could make this big career change, and she put up with my long hours of studying necessary to make it happen.

Identification of Blood Vessels in Cortical Bone Pores utilizing DCE-MRI and HR-pQCT

Matthew R. Gibbons

**ABSTRACT**

**Purpose:** Various diseases, such as Type II Diabetes (T2D), impact the microarchitecture of bones. DCE-MRI and HR-pQCT have been used to investigate cortical bone structural changes and to understand the role blood vessels have in the development of T2D-related pathological porosity in cortical bone. The purpose of this project was to look at the cortical bone porosity, and determine the contents of the pores (whether or not they had affiliated blood vessels), so as to better understand the mechanisms driving pathological bone porosity. To this end, image processing routines were developed to quantify bone porosity and to determine blood vessel location and volume fraction.

**Methods:** Results from an existing DCE-MRI and HR-pQCT image processing protocol (pipeline 1) were used in this study. As part of pipeline 1, the MRI and CT images underwent a global rigid registration. Pipeline 1 also provided masks for the CT cortical bone, the blood vessels, and the bone pores. Image pipeline 2 was developed through this thesis project. Pipeline 2 has a set of threshold and dilation/erosion steps to create a mask for the MRI cortical bone. It also performs non-rigid registration of bone masks and completes registration of vessels to pores with a piecewise rigid algorithm. The overlap of the registered vessel mask with the pore mask determines the final properties and biomarkers of the blood vessel network. Numerical and physical phantoms were used to characterize the algorithms by allowing a comparison to ground truth.

**Results:** In bone data artifacts are visible in the MRI bone masks. The imaging pipeline overcomes these and increases MRI to CT bone Dice coefficients from 0.8 to 0.9. Blood vessel alignment, as defined by vessel voxel overlap with pore voxels, is improved with vessel overlap increasing from 20% to 90%, and vessel voxel overlap increasing from 8% to 40%. Analysis of 12 distal and ultra-distal tibia data sets did not show a statistically significant difference between normal and T2D patients (mean ~ 0.3% for each with $p = 0.4$). A numerical phantom study provided metrics for pipeline 2 success. It indicated that after pipeline 1 offsets between vessels and pores should be < 15 voxels and pore densities should be < 20%. A physical phantom study showed capability to identify vessels with diameters as small as 300 $\mu$m.

**Conclusions:** Positive results with bone and phantom data indicate a proof of concept for the general approach as well as the implemented algorithms. Pipeline 2 achieved high alignment fractions for blood vessels and pores. The analysis of both bone and phantom data has led to the definition of metrics and identification of specific algorithm deficiencies. Future work on these items should result in a robust image analysis pipeline for most data sets and a set of useful metrics to distinguish problematic data sets. These algorithm improvements along with analysis of more data sets will be needed to ascertain whether there are statistically significant differences between populations for cortical bone vessel densities.

# Table of Contents

## List of Tables

## List of Figures

# 1 INTRODUCTION

The skeleton provides shape and structure to our bodies, and the bones perform a wide range of essential functions. To perform all of these functions, bones are organs composed of living tissues. The skeletal system is as complex as any other organ within the human body.

The three main components of bone are: cortical (compact) bone, trabecular (spongy) bone, and marrow [1]. Compact bone is the densest, hardest, and heaviest bone tissue, located on exterior bone surfaces. It provides most of the support for the body. Present within the compact bone are canals filled with nerves, blood vessels, and bone marrow. The trabecular bone, within the bone interior, has a characteristic 'honeycomb' architecture consisting of many irregular-shaped trabeculae. The space between trabeculae are also filled with marrow, nerves, and blood vessels. The bone marrow is within the central cavity of long bones. Marrow provides the microenvironment for various types of stem cells including hematopoietic stem cells (which differentiate into various immune cells and red blood cells), and mesenchymal stem cells (which differentiate into adipocytes, osteoblasts, osteoclasts, etc.) [2].

Bones are not static. They maintain a homeostasis where ossification (bone formation) and resorption (bone removal) constantly renew the bone structure in the process of remodeling. An imbalance with more resorption can decrease the bone density and volume while increasing porosity. This will decrease bone strength and increase fracture risk.

Various diseases (Human Immunodeficiency Virus (HIV) or diabetes), as well as life stages (menopause or aging) affect bone biology, morphology and microarchitecture. The HIV virus can infect the bone impacting the osteoblasts' ability to carry out bone formation functions, plus adverse effects have been reported with various antiretroviral treatments [3]. Bone structure and function can be modified by the enhanced glycation environment created by diabetes, including increased mesenchymal stem cell apoptosis [4] [5]. Post-menopausal women can be negatively impacted by reduced levels of estrogen, decreased osteoblast (bone formation) activity, and increased osteoclast (bone resorption) activity, resulting in decreased bone density and increased porosity [6] [7]. Patients with bone degenerative diseases may have higher fracture risk even though bone density may not be significantly worse.

Studies in the Kazakia Lab use Dynamic Contrast Enhanced Magnetic Resonance Imaging (DCE-MRI) and High Resolution Peripheral Quantitative Computed Tomography (HR-pQCT) to

investigate cortical bone structural changes. DCE-MRI identifies blood vessels while HR-pQCT shows the mineralized bone components.

In the past, Dual-Energy X-ray Absorptiometry (DXA) was used to assess Bone Mineral Density (BMD) as an indirect measure of bone fracture risk. However, BMD levels do not provide the bone architecture / microstructure information needed when studying bone pores. In recent years, HR-pQCT has taken precedence (Fig 1a) [8]. HR-pQCT acquires images based on the same principles as traditional QCT, but at much higher resolution, allowing imaging of pores within the bones. High resolution impacts acquisition time with scan averages of ~3 min. Despite the longer scan time, HR-pQCT radiation dose is not reported as higher in part due to the small, peripheral volumes scanned [9].

Anatomic information of blood vessels is obtained with DCE-MRI [10] [11]. DCE-MRI analyzes the temporal enhancement pattern of a tissue after injecting a contrast agent into the body. The contrast agent used for DCE is a paramagnetic gadolinium (Gd) chelate which decreases the T1 of protons [11]. As a result, tissues and vessels that take up Gd will have a lower T1 value, and display a higher signal after T1-weighted MRI imaging. After injection, Gd will leak into the extracellular space of tissues, but cell membranes prevent uptake into cells. Finally, Gd returns to vessels from extracellular space and wash out occurs via the kidneys (Fig 1b).

a)  b) 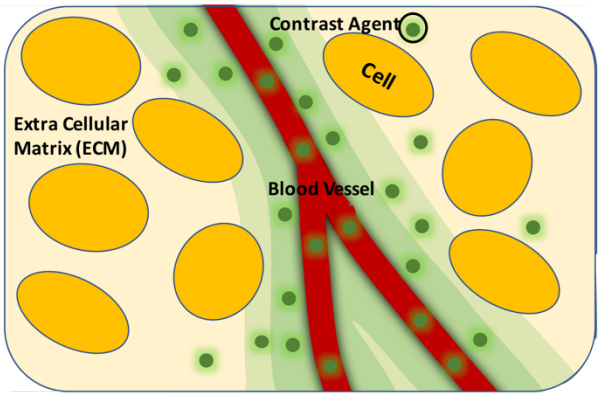


**Fig 1:** a) HR-pQCT scan and b) Gd process in the body

Since DCE-MRI has poor resolution compared to HR-pQCT, the MRI observed blood vessels will appear larger than they actually are. Simply counting blood vessel voxels and comparing to pore voxels

will result in an incorrect assessment of blood vessel density. As part of the image analysis pipeline, blood vessels are associated with specific pores. The intent is to correct the blood vessel volumes for a more accurate assessment. Since parts of blood vessels may be missing because of poor MRI resolution, blood vessel to pore alignment may also enable estimates to fill in unresolved blood vessel segments.

The purpose of this project was to investigate the cortical bone porosity, and determine the contents of the pores (whether or not they had affiliated blood vessels). This capability will support subsequent research to better understand the mechanisms driving pathological bone porosity. To this end, image processing routines were developed to quantify bone porosity and to determine blood vessel location and density. Objectives included creation of MRI cortical bone masks, confirming alignment of MRI and CT images, aligning MRI blood vessel masks and CT pore masks, trimming the blood vessel masks consistent with the pore mask envelope, and reporting biomarkers such as blood vessel volume fraction of the resulting blood vessel networks.

## 2 METHODS

The data sets for this study are from tibia acquisitions coordinated by the Kazakia lab at the UCSF Department of Radiology and Biomedical Imaging in China Basin [12]. Reconstructions were made of the distal and ultra-distal tibia in a trial study of patients with Type II Diabetes (T2D) and healthy controls [12] [13]. For CT, a clinical HR-pQCT scanner (XTremeCT, Scanca Medical AG, Bruttisellen, Switzerland) was used. The x-ray source was set with voltage 60 kVp and current 900 μA. The acquisition FOV was 126 mm with 750 projections to achieve a resolution of 0.082 mm x 0.082 mm x 0.082 mm [14]. The MRI scanner was a 3T wide-bore system (GE Healthcare, Chicago, USA). The DCE-MRI protocol was a spoiled gradient echo (SPGR) pulse sequence with Frequency Encoding Field-of-View (FOV) 12 cm, and Phase Encoding FOV 9 cm. The acquisition resolution was 0.23 mm x 0.23 mm x 0.5 mm. The contrast agent, Gadavist, was administered, 0.1ml/kg, intravenously at 2ml/s. After a 1 min delay, 18 MRI acquisitions were made at 30 sec intervals [13]. MRI and CT acquisitions were completed within the same day so no change in the bone structure was expected.

The image analysis for this project consists of two parts. The first part (pipeline 1) is an image processing pipeline developed in the Kazakia lab by Dr. Po Hung [13]. The DCE-MRI and HR-pQCT data are the input. Image masks for cortical bone, pores in the cortical bone, and blood vessels in the cortical

bone are the outputs. The image analysis developed for this thesis (pipeline 2) consists of generating an MRI bone mask, registering MRI and CT bone masks, and quantifying blood vessel vs pore locations.

### 2.1 Image Processing for vessel identification (Pipeline 1)

Pipeline 1 has three parts: a) registration, b) mask generation, and c) segmentation [12] [13]. In the registration step a normalized mutual information registration technique is implemented using FSL software [15]. The target image is the first MRI acquisition which is prior to contrast affecting the imaging. The subsequent DCE-MRI and HR-pQCT images are the source images registered to the target. Next cortical bone and pore masks are created from HR-pQCT data using a segmentation algorithm that determines endosteal and periosteal boundaries of the cortical bone [16] [17]. The cortical bone is used as a mask on the DCE-MRI data so only voxels within the cortical bone are identified as blood vessels.

The blood vessels enhance over the course of the DCE-MRI acquisition, while the marrow fat and bone do not. Since automated analysis must be implemented on each voxel, the enhancement is not averaged over a manually selected Region-of-Interest (ROI). Noise in this non-averaged signal makes classification, based only on the maximum enhancement ratio, prone to error. Thus, several features of the enhancement are extracted for further processing.

The first feature is the primary component from a Principal Components Analysis (PCA) [18] of DCE-MRI data that has been filtered to bring out vessel-like objects. The filtering algorithm, based on work by Frangi, et. al. [19], uses the image Hessian matrix (a second order kernel) to provide local structure information. It calculates a vesselness measure for each voxel from the structure information. This is a multiscale algorithm for detecting vessels of various diameters. A range of scale factors must be provided. Factors from 0.75 to 1.25 appear to work well for vessel diameters from 1 to 10 voxels. The PCA interrogates the complete time series of vesselness images and returns principal components, characterizing the enhancement curve. Other extracted features are the Area Under the Curve (AUC), the standard deviation of the curve, and the sum of the local differences between each time point. These four features are processed by a k-means clustering algorithm [20]. The voxels in the k-means group with the largest vesselness are designated as blood vessel voxels. A blood vessel mask is generated from these voxels.

### 2.2 Registration of blood vessels to pores (Pipeline 2)

**Mask analysis:** Bone masks are generated from pre-enhancement MRI images through the following steps (Fig. 2):

1) Determine a threshold from a center ROI intensity $(marrow_{average} - minimum_{intensity})/3 + minimum_{intensity}$. Set cortical bone equal to 0 by creating a binary image from the raw MRI data using the threshold. Because of MRI image noise the cortical bone will not always form a contiguous ring. To ensure bone continuity, a narrow annulus from the CT cortical bone mask is nulled in the MRI image. The narrow annulus is generated by performing a skeletonization operation on the CT mask [21].
2) Set the background equal to 0 outside the bone with an operation using the CT cortical bone mask.
3) Perform a fill operation to fill holes in the trabecular bone interior that remain after previous operations.
4) Use an open operation to remove non-zero voxels caused at the interface between the CT and MRI bone outer boundaries. The non-zero voxels occur because the CT and MRI edges do not align perfectly. This step creates a mask of the MRI trabecular bone.
5) Add the inverse of the mask from step (1) to return the cortical bone to the MRI bone mask.
6) Perform a fill operation to remove any holes that occurred due to operations (4) and (5).
7) Smooth the outer boundary with a close operation and subtract the trabecular mask of step (5) to complete the MRI cortical bone mask.

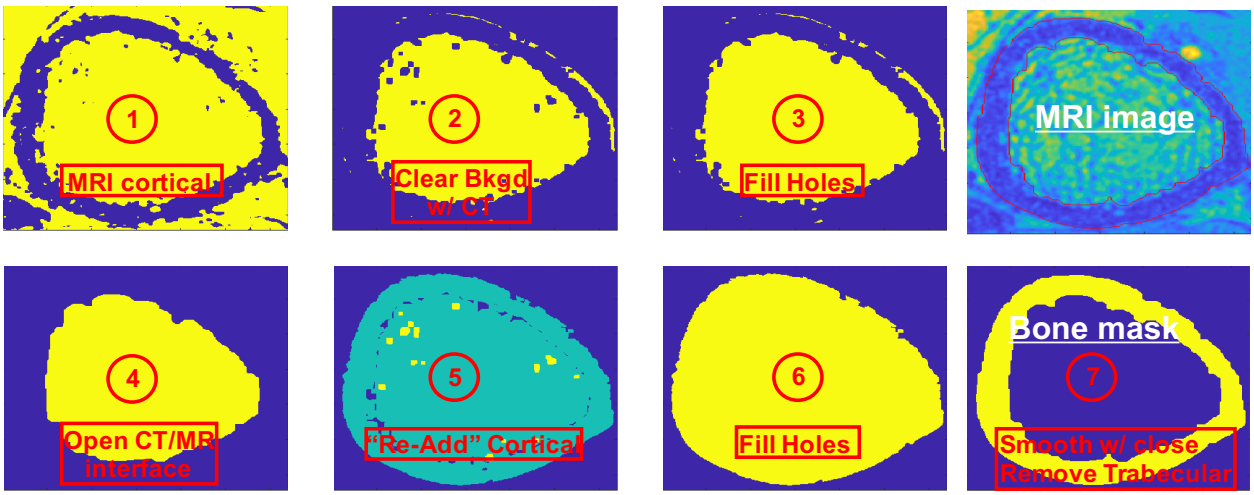


**Fig 2:** Steps in the MRI bone mask algorithm

The MRI and CT bone masks were compared qualitatively and quantitatively. An outline of the MRI bone mask was generated through edge detection using the Laplacian-of-Gaussian algorithm. The edge was added to the raw MRI and CT images for visual, qualitative assessment. The difference between masks was quantified with the DICE coefficient.

$$DICE = 2\,(MRI \cap CT)/(MRI + CT) \quad (1)$$

### 2.3 Blood vessel and bone pore analysis:

Using the cortical bone masks from both CT and MRI, steps to align the blood vessels with the pores were preformed: a) non-rigid register the MRI mask to the CT mask, b) apply displacement matrix to the blood vessel mask, c) define volumes of interest (VOI) around the blood vessels, d) piecewise register the vessels to the pores using the VOIs, and e) calculate the vessel to pore overlap.

#### 2.3.1 Non-rigid registration

Due to artifacts in the MR acquisition, deformation was evident in the cortical bone mask from MRI as comparted to CT. Demons non-rigid registration (Matlab imregdemons() [22] [23]) was used on the MRI mask to mitigate this issue. Since the masks were of similar shape and already overlapped from the rigid registration of pipeline 1, the additional deformation was well within the capability of the Demons algorithm. The operation moved the MRI pores and vessels closer to appropriate locations in the CT pore mask. This is necessary for cases where the MRI bone appears thicker than the CT bone. The calculated registration displacement matrix was then applied to the blood vessel mask.

#### 2.3.2 Piecewise rigid registration

Because of the tight alignment required in this project, the non-rigid registration does not achieve sufficient accuracy. The next step was a piecewise rigid registration of the vessel mask. The vessels were identified by segmentation and filtered according to size. Those smaller than 100 voxels were not used for this final registration step. The mask was divided into pieces by defining sub-VOIs that extend a defined radius around the blood vessels. If sub-VOIs intersect, they were combined. Limits were defined in the Cartesian coordinate system so the final VOIs were formed as hexahedra. The code started with a 14 voxel sub-VOI radius and reported the resulting sizes of the final VOIs. The user was queried to provide changes to the defined radius should the final VOIs be too large or small.

Before registration the pore mask was modified to deal with discrepancies between the MRI and CT bone masks where parts of vessels may exist in the trabecular compartment. Voxels, that were within the trabecular compartment and < 6 voxels away from vessels, were added to the pore mask. These added volumes were small, intermittent patches around the endosteal boundary of the cortical bone since few vessels resided near the boundary. These trabecular voxels were not counted for purposes of vessel overlay fraction, vessel volume fraction in cortical bone and other parameters. With the VOIs and modified pore mask defined, rigid registration of the vessel mask to the pore mask was performed within each VOI by the Matlab imregister() function [22] [24].

### 2.3.3 Calculation of properties and statistics

Vessel to pore alignment was inspected in several ways. Visual inspection of 3D renderings and 2D slice images provided a qualitative assessment of vessel and pore features. Overlap was defined as voxels that were intersections of both the vessel and pore masks. Before calculating overlap, the pore mask was expanded by adding voxels that both overlap the vessel mask and have BMD one standard deviation below the mean BMD for cortical bone. The fractional overlap was quantified between vessels and pores with voxel counts and segmented vessel counts. Good alignment should exhibit an increase in both these quantities. However, 100% overlap of vessel voxels with pore voxels was not expected. Since MRI resolution was worse than CT resolution, the vessels generated by the image pipeline may extend beyond their actual physical volume. Clipping of the vessel volume, so vessels fit within the pores, was a desired function of the pipeline.

Once the aligned and reduced blood vessel mask was finalized, the characteristics of the blood vessel network were calculated. Voxel counts and properties provide biomarkers, specifically: blood vessel volume fraction compared to cortical bone and pores; vessel volume fraction within the lamina of the cortical bone (endosteal, mid, and periosteal); and BMD in bone, pore, and vessel regions. Vessel volume fractions were calculated as the ratio of the number of vessel voxels divided by total number of voxels within the cortical bone boundary or total number of pore voxels. Means of the properties were calculated from the data sets and compared against various factors: control vs T2D patient, distal vs ultra-distal tibia, and BMD region. Statistical significance was calculated by p-value using the MATLAB ttest2(). Box plots, generated by the MATLAB function boxplot(), were employed to display distribution

comparisons.

### 2.4 Calibration and repeatability:

Because in vivo data is being analyzed, there was no “ground truth” for blood vessel location or size to determine the efficacy of the registration pipeline. To quantify the pipeline’s ability to correctly achieve vessel alignment, experiments were performed on known configurations with numerical and physical phantoms. Additionally, the physical phantoms provided resolution calibration data. The image analysis pipeline was investigated to determine whether it was robust to variation in MRI scan data. The effect of repeat MRI scanning on biomarkers for vessel volume fraction was analyzed.

#### 2.4.1 Numerical phantom

The blood vessel network derived from DCE-MRI does not capture the complete anatomic network due to resolution limitations and varies depending on the features input to and groups selected from the k-means algorithm. The CT data provides a more accurate estimate of the pore network, but still is not a perfect representation. With this in mind, a phantom of numerically generated pore and vessel networks embedded in a cylindrical bone structure was created.

The phantom is shown in Fig. 3. The image domain is 301 x 301 x 50 voxels. For the CT image an annulus bone mask was defined with a radius of 85 voxels and thickness of 30 voxels. Pores were defined as 3 x 3 x 5 voxel columns. The positions of the pores were defined randomly within the volume of the bone mask with a volume fraction selected by the user to be a specified fraction of the total bone volume. Pores to accommodate blood vessels were also added to the pore mask. Blood vessels were square 5 x 5 columns in four groups with 1, 2, 3, and 4 vessels, respectively. The four groups tested the effect of the pipeline on singular or clustered vessels. Six vessels were the full 50 voxel height while four of the vessels were ½ height resulting in 10000 vessel voxels in total. The MRI bone mask was 10% larger than the CT bone mask with a radius of 94 voxels and thickness of 34 voxels. The difference in size was imposed to determine whether the pipeline was robust to errors in MRI to CT calibration. If the non-rigid registration correctly morphed the MRI bone into the CT bone shape, the reduction in vessel volume should be $(101^2 – 71^2) / (111^2 – 78^2) = 0.83$. So, the number of vessel voxels should be 8300.

The success of the vessel alignment pipeline was characterized as a function of mis-registration between the MRI and CT data as well as pore volume fraction in the cortical bone. In this study, the MRI

data was misaligned by rotation. As with the real data, the alignment of vessel voxels with pore voxels was characterized; however, this did not quantify whether the vessels were aligned with the correct pores. Because this was a numerical phantom with known properties, calculation of the overlap fraction with the true vessel positions was possible as a metric of model accuracy. The overlap fractions were tabulated for rotation angles from $0^{o}$ to $18^{o}$ and pore densities from 0% to 60% in order to determine conditions where pipeline 2 successfully aligned the MRI vessels to correct pore locations.

a) 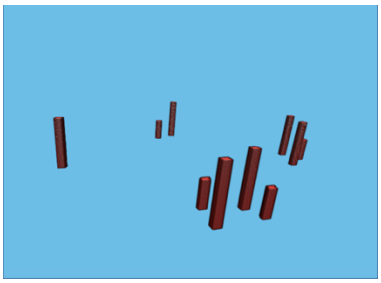 b) 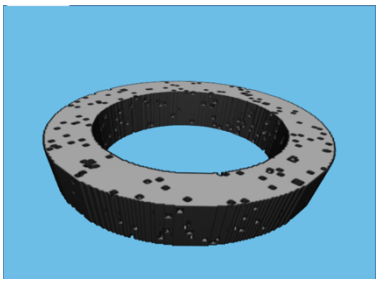 c) 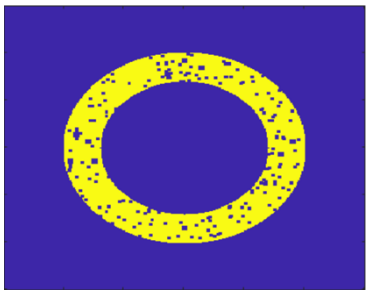

**Fig 3:** The numerical phantom a) 3D blood vessels b) 3D bone with pores and c) 2D bone with pores

### 2.4.2 Physical phantom

The objective was to use a phantom in both DCE-MRI and HR-pQCT experiments to investigate and quantify the precision and accuracy of the image analysis (registration) pipelines. Optimally, a phantom should have attenuation, contrast, enhancement, and geometric characteristics similar to the distal / ultra-distal tibia (including pore or vessel type structures). For the purpose of characterization and calibration, a geometry much simpler than a pore or vessel network is desired. The same biomarkers, as calculated for actual subjects, such as pore or vessel volume fractions were evaluated.

PET phantoms available in the UCSF Radiology and Biomedical Imaging Department had useful properties for this set of experiments. One of these was the Small Animal NEMA PET Phantom NU4 (Fig 4a) [25]. The dimensions of the phantom included an outer dimension of 33.5 mm and a cylinder length of 63 mm. There were three fillable chambers in the phantom, one with an inside diameter and length of 30 mm, while the other two had inside diameter of 8 mm and length of 14 mm. The phantom hot spots were channels of 1, 2, 3, 4, and 5 mm in diameter. The cross-section dimensions were similar to those for the distal tibia while the smallest hot spots were large compared to cortical bone blood vessels. A smaller

phantom, provided with a MILabs VECTor4 PET/SPECT/CT [26] system was also imaged (Fig 4b). It had an outer (diameter 20 mm) and an inner (diameter 12 mm) cylinder. The inner cylinder held a “hot rod” phantom with arrays of channels having diameters approximately 500, 400, 350, 300, 250, and 220 μm. Each array was a triangular pattern with 6, 10, 10, 10, 15, and 15 channels, respectively (Fig 4c). These hot spot arrays were a better size mimic for a vessel network in cortical bone. The phantoms were composed of PMMA which has attenuation similar to water for x-rays. In MRI, the PMMA signal was low which is similar to the behavior of bone [27]. The phantoms were placed in Styrofoam forms shaped to maintain a consistent orientation. The whole configuration was then held in a plastic container with a sealable lid as shown in Fig 4d. Three scans were performed as detailed below: HR-pQCT scan (1), MRI scan (2), and MRI scan (3). The scan parameters were the same as those defined in the introduction.

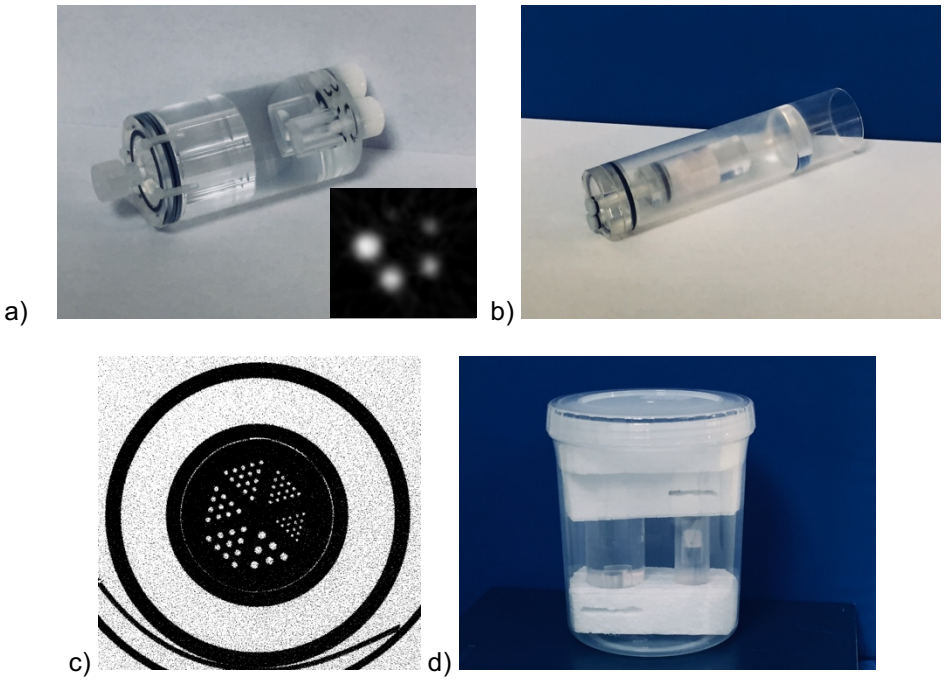


**Fig 4:** PET phantoms a) NEMA NU4 phantom, b) hot rod cylinder phantom, and c) phantom container

CT experiment: The HR-pQCT scan (1) was performed with the phantom and vertical axes aligned. The phantom was empty so that phantom walls were attenuating relative to the non-attenuating chambers. This was a mimic for bone vs tissue contrast; however, the PMMA was not as attenuating as bone. The purpose of this experiment was for comparison with the MRI results not as an additional

calibration for the HR-pQCT.

MRI experiment: The SPGR MRI scans (2) and (3) were performed with the phantom and vertical axes aligned. The NEMA phantom and the inner cylinder of the small phantom were filled with contrast enhancing (CE) solution. Contrast concentrations needed to achieve enhancement similar to patient scans were calculated. Together both images were used to mock up an enhancement response where normalizing by the baseline image would leave only the enhancement. Desired CE concentrations were achieved by diluting Magnevist (Gd-DTPA) solutions with saline (table 1). The outer cylinder of the small phantom was filled with saline, and the container for the phantoms was filled with water. This provided contrast with the PMMA walls of the phantoms in a manner similar to tissue vs bone [27].

It was necessary to adjust the contrast concentrations to provide appropriate enhancement for this static phantom experiment. The SPGR MRI sequence had TR / TE = 12ms / 4ms. For the solution, T2 should be substantially larger than TE, and T1 should not be too large compared to TR. With T1 in the range of 100 ms to several hundred ms, bright and intermediate brightness can be achieved from the T1 response. Plus, T2 would be significantly larger than TE so T2 and T2* relaxation should not adversely affect the signals.

The Gd concentrations needed to achieve the target T1 and T2 were calculated. The observed relaxation rate, $T_{obs}$, depends on the intrinsic relaxation rate, T1, and the impact due to the specific relaxivity of the Gd, r1 and r2 [28]. The relationship is

$$1/T_{obs} = 1/T_1 + 1/T_C \quad (2)$$

$$1/T_C = r1 \cdot (Gd\ concentration) \quad (3)$$

Magnevist has r1 = 3.9, r2 = 5.1, and concentration = 0.5 mmol / L [28]. For water T1 = 4000 ms, and T2 = 2000 ms. Table 1 lists example relaxation times for various Magnevist dilutions. Solutions 1:200 and 1:500 were used in the phantom experiments.

**Table 1:** Estimated relaxation times for Magnevist diluted in saline

| Gd concentration | T1_obs | T2_obs |
|---|---|---|
| 1:100 | 50.6 | 37.7 |
| 1:200 | 100.0 | 74.1 |
| 1:300 | 148 | 109.1 |
| 1:500 | 241 | 175.4 |

The plan for the phantom scan was to perform scan (2), refill the phantom with a different Magnevist dilution, and perform scan (3) in the same session. The MRI had a software interrupt at the beginning of the session which left insufficient time during the session for scan (3). Scan (3) was performed later in the same day; however, the prescan calibration was not the same for the two scans. Because of this a procedure was implemented to deal with the water and PMMA having different relative intensities between scan (2) and scan (3). For the purpose of creating a DCE pseudo-time sequence, we performed a linear fit to match the water and PMMA between the two data sets. The resulting difference image nulls out water and PMMA on average. A net signal still exists in the contrast agent volumes where scan (3) had higher signal than scan (2). With this methodology, a data set was generated which was processed through the image analysis pipeline. This data set could not be compared with calculations for relative intensities of the two contrast agent concentrations.

Spatial calibration: The reconstructions of the phantom will quantify the resolution for objects in the MRI vs the CT images. Given the regular shape of the phantom, dimensions can be measured and compared to expectation. In the results section, the spatial characteristics of the small diameter channels with contrast agent were tabulated since the purpose of the channels is to mimic blood vessels.

Image analysis: With scans (1), (2), and (3), we had a set of data equivalent to that used for the project image analysis pipeline. The MRI-DCE data set was created by taking the first two time points from data set (2) (the baseline) and taking time points 3 to 18 from data set (3) (enhanced). The result is a step function enhancement curve which still maintains the variability of 18 separate acquisitions. Then we processed the data through the analysis pipeline and checked the efficacy of each step by comparing to the known properties of the phantom. As noted in the calibration section, this process was more tractable with the phantom than with an irregular shaped cortical bone and pore/vessel network. The main steps performed for the pipeline remain the same with slight modifications to deal with phantom data instead of distal tibia data:

1) Generation of CT cortical bone and pore masks: The phantom data was not processed through the HR-pQCT software. It was processed in MATLAB by defining a 75% intensity threshold for PMMA. This leaves a mask of only PMMA with air nulled out. The mask is filled resulting in a cortical bone mask of all

voxels within the outer boundary of the phantoms. The inverse of the PMMA mask within the boundary of the bone mask defines the pore mask.

2) Rigid registration of MRI to CT: The MATLAB imregister() function was used to transform the MRI data to align with the CT data on a CT resolution mesh. Since the phantoms are regular cylinders, the registration routine does not have large irregular structures to use for rotation alignment around the central axis. Only the orientation of the small channels causeds rotational asymmetry. This global symmetry was not a registration issue for the tibia data. To overcome this issue, manual rotation was applied before registration to get the channels closer to alignment. The global rigid registration did not provide final alignment. The capability of the image pipeline to complete the alignment was investigated.

3) Generation of vessel mask from DCE-MRI: The routines of image pipeline 1 were used. The Frangi scale range was modified to be 2 to 10 for the large phantom since the channels have large diameters from 1 mm (12 voxels) to 5 mm (60 voxels).

4) Generation of cortical bone mask from MRI: The routines of image pipeline 2 were used. They were slightly modified to completely fill the cortical bone mask. The original routines were designed assuming a trabecular cavity inside the cortical bone.

5) Registration of vessel mask to pore mask: The routines of image pipeline 2 were used.

6) Calculation of properties (vessel overlap with pores, pore volume fraction, and vessel volume fraction): The routines of image pipeline 2 were used. Since more accurate channel sizes are available, these were compared to the VECTor4 CT data as a ground truth [26]. Dice coefficients for the channels in the large phantom were calculated. With the small phantom, the 6 channel arrays were segmented using manually placed wedge volumes. The channel volume derived from the pipeline was compared to the ground truth for each wedge.

#### 2.4.3 MRI Reproducibility

It was not feasible to get multiple DCE-MRI scans from the same patient. However, the time series data already available could be used to mock up separate scans. Reproducibility of vessel registration and count results were tested by splitting the DCE-MRI data into separate sets. The sets of enhancement images were defined as all the time points vs only odd time points vs only even time points. The odd and even time points consisted of independent acquisitions. The image pipeline for blood vessel

designation generated slightly different blood vessel networks for each data set. Since the filtered (alternating time point) data sets had only a subset of data, they created relatively truncated blood vessel networks. For this reason, comparison between even and odd was more appropriate than comparison of odd or even to the full data set. Each case was processed through the vessel/pore alignment pipeline and the biomarkers (blood vessel volume fraction) in the cortical bone were tabulated.

## 3 RESULTS

### 3.1 DCE MRI

The dynamic MRI has 18 time sequence data sets with a time step of 30 seconds. An example enhancement image from one slice is shown in Fig 5a. Several circular hot spots are visible in the image as yellow on the color map. Some are within and some external to the bone perimeter. The largest is a vessel just outside of the bone. This vessel was selected as an ROI from which to generate the enhancement curve shown in Fig 5b. The enhancement peaks add about a factor of 2 (100%) above the baseline. The rise time is < 1min with the peak occurring at 2 min after the start of taking data. Only partial washout (~20% decrease from the peak) occurs by the end of data acquisition at 8.5 min.

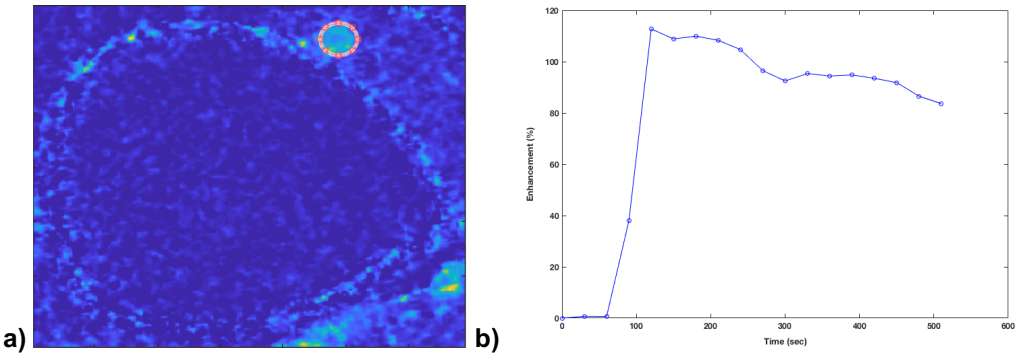


**Fig 5:** a) DCE MRI image and b) Enhancement (%) curve

### 3.2 MRI mask characteristics

Fig 6 compares MRI and HR-pQCT masks. The MRI boundary generally follows the cortical bone edge visible in the CT image. In some areas, the MRI bone is deformed away from the CT bone. Although misshapen, these regions appear to represent the bone in the MRI data since the pore structure correlates with that visible in the CT data. The extent of overlap was quantified by dice coefficients

calculated over all slices in each data set (Table 2). As expected the dice coefficients increase after the non-rigid registration step from an average of 0.82 to 0.90. The ultra-distal bones with thinner cortical bone exhibit slightly lower (~4%) Dice coefficients than the distal.

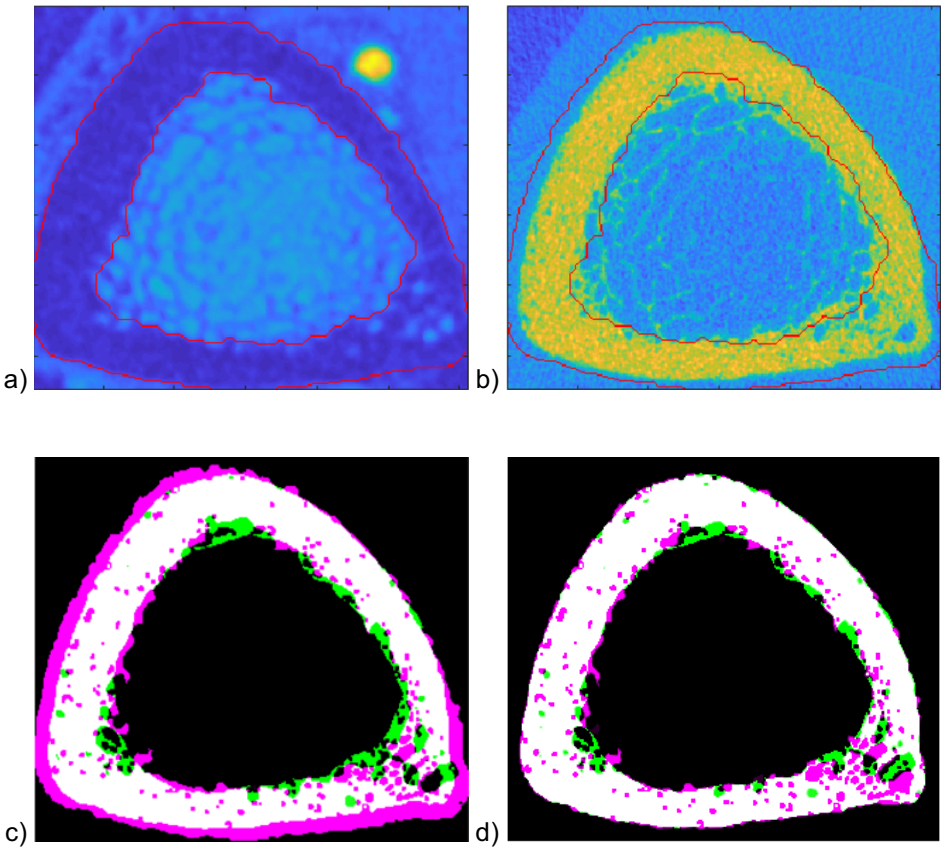


**Fig 6:** Image comparison of a) MRI, b) CT with MRI bone boundary highlighted, c) overlay of bone + pore masks from MRI and CT before non-rigid registration, and d) overlay of bone + pore masks from MRI and CT after non-rigid registration

**Table 2:** Dice coefficients (MRI vs CT bone masks)

| Mask | Distal | | | | | | Ultra Distal | | | | | |
|---|---|---|---|---|---|---|---|---|---|---|---|---|
| Initial | 0.864 | 0.879 | 0.814 | 0.895 | 0.873 | 0.810 | 0.802 | 0.721 | 0.776 | 0.825 | 0.816 | 0.742 |
| After | 0.938 | 0.950 | 0.905 | 0.951 | 0.953 | 0.916 | 0.875 | 0.853 | 0.859 | 0.898 | 0.911 | 0.807 |

### 3.3 Vessel Overlay of Pores and calculated cortical bone characteristics

Examples of blood vessel and pore mask overlap are shown in Fig 7. The red voxels are vessels and the yellow voxels pores. Fig 7a is a 3D rendering with a wedge removed from the cortical bone showing blood vessels embedded in the pores. Upon visual inspection of the 3D images the vessels

appear to fit into pore volumes which have an appropriate shape including branches that are present in some vessels. Often the vessels and the pores have breaks along their length which may be imperfections in the respective masks as opposed to the real objects. Fig 7b is an image of blood vessels including only those voxels that simultaneously overlap with pore voxels. Several vessels of considerable length are visible. Many vessels are small and may be segments of longer vessels. Such vessels may have diameters mostly below the resolution limit so only intermittent sections become detectable.

a) 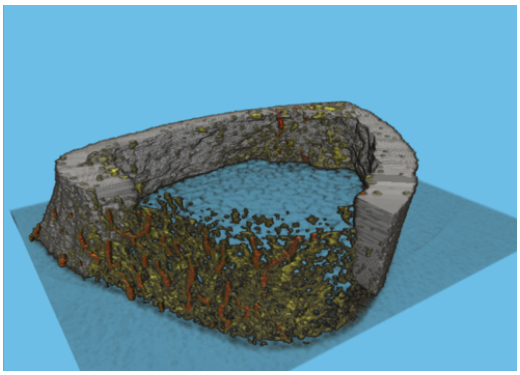 b) 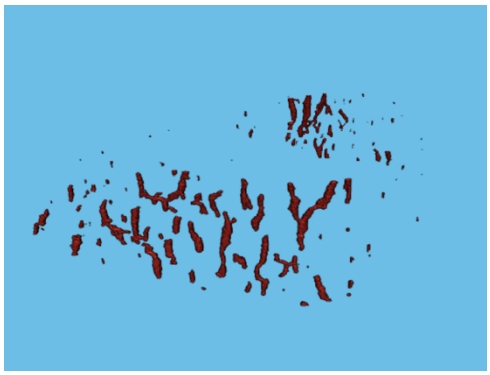

**Fig 7:** 3D renderings a) blood vessels (red), pores (yellow) with wedge removed from cortical bone and b) blood vessels only

Fig 8 highlights several aspects of the vessel counts for the 12 data sets analyzed. In Fig 8a, the number of vessels is plotted vs the number of voxels in each data set. The average number of voxels per vessel (~40) is consistent across the data sets as evidenced by $R^2$ = 0.93 for the linear fit. The impact of size filtering before the registration steps is shown in Fig 8b. Filtering decreases the number of vessels by ~4x; however, the number of voxels only decreases by ~25%. This is due to the distribution of vessel sizes with the removed vessels having an average size of ~20 voxels while the remaining vessel average is ~200. The fraction of blood vessels and vessels voxels that overlap with pore voxels is plotted in Fig 8c. The voxel fraction mean increased from 8% to 40%, and the vessel fraction mean increased from 20% to 90%. A representative displacement of the vessel network during the alignment pipeline is visualized in Fig 8d. The network is shown before and after alignment in the image. The displacement ranges from ~4 to 10 voxels.

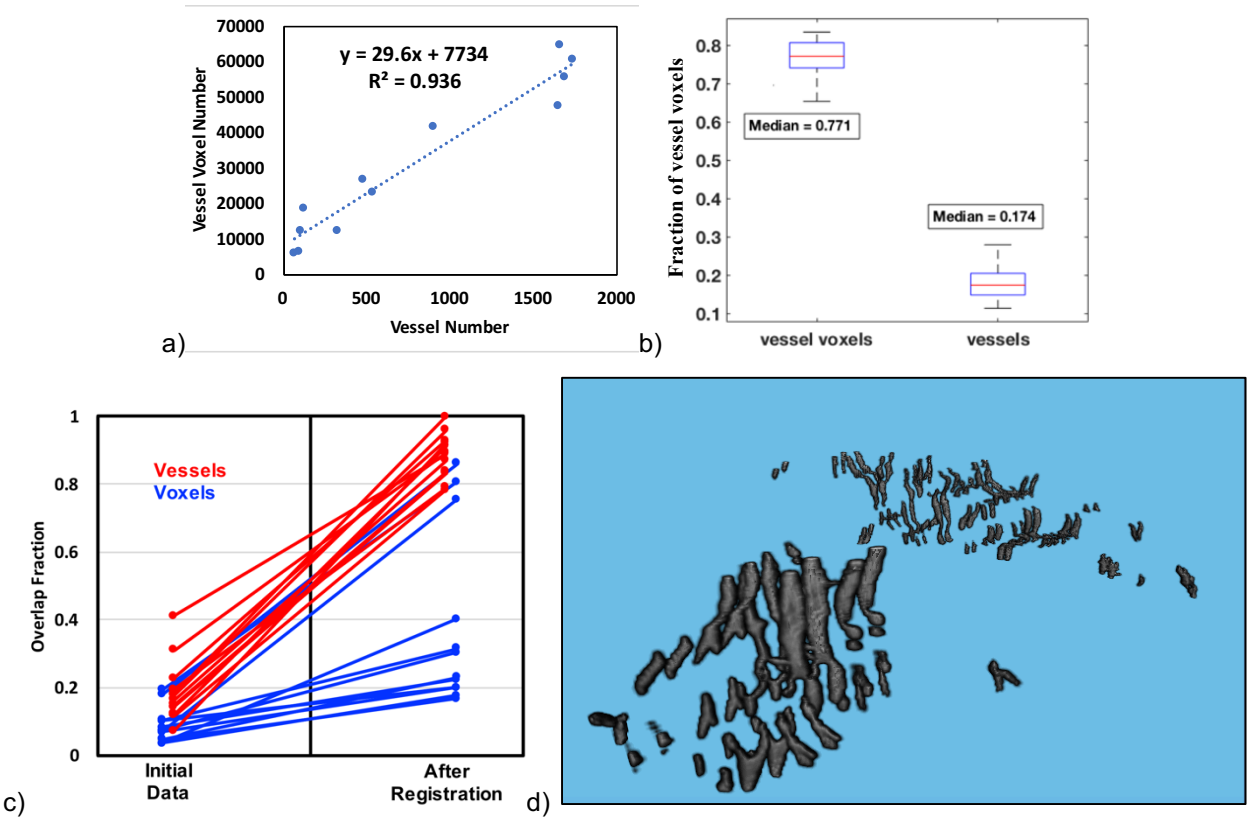


**Fig 8:** Registration results a) counts of vessels vs voxels, b) remaining fraction of voxels after filtering and non-rigid registration, c) vessel alignment w/ pores, and d) vessel network from before and after the alignment pipeline combined in the same image

The overlap fraction after the alignment pipeline remains low for a majority of the data sets. Several of the data sets exhibit the characteristics shown in Fig 9. Many voxels identified as vessels are far from any pore voxels. This is a contributor to low alignment fractions. Only severe, unrealistic deformation of the cortical bone shape would result in overlap of vessels with pores.

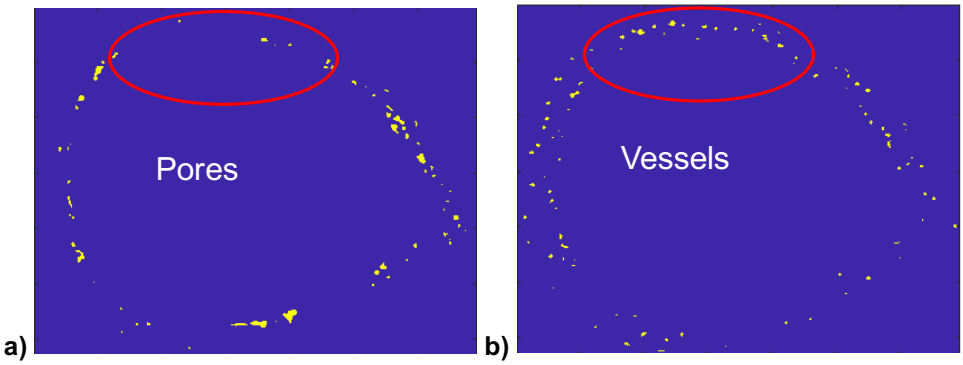


**Fig 9:** Comparison of a) pore and b) vessel positions for a low overlap fraction data set

Biomarkers for subjects in the Type II diabetes (T2D) trial were summarized for distal and ultra-distal tibia data from six subjects (4 normal and 2 patients). The vessel volume fraction (vessel voxel counts normalized by either pore voxels or all voxels within the cortical bone mask) of normal subjects and patients was compared. In both cases the mean for pores (normal 0.062, T2D 0.034, p-value 0.12) and bone (normal 0.0036, patients 0.0028, p-value 0.41) was larger for normal subjects than for patients; however, neither met statistical significance of $p < 0.05$. Statistical significance was evident across the whole population in the difference between the distal and ultra-distal portions of the tibia. The comparison was for vessels normalized by pores (distal 0.065, ultra-distal 0.032, p-value 0.057) and pores normalized by bone (distal 0.053, ultra-distal 0.098, p-value 0.025). The thinner ultra-distal cortical bone had a lower vessel volume to pore volume but a higher pore volume to cortical bone volume. The vessel volume to bone volume was almost the same. In both regions, the volume fraction of pores to cortical bone was < 15%.

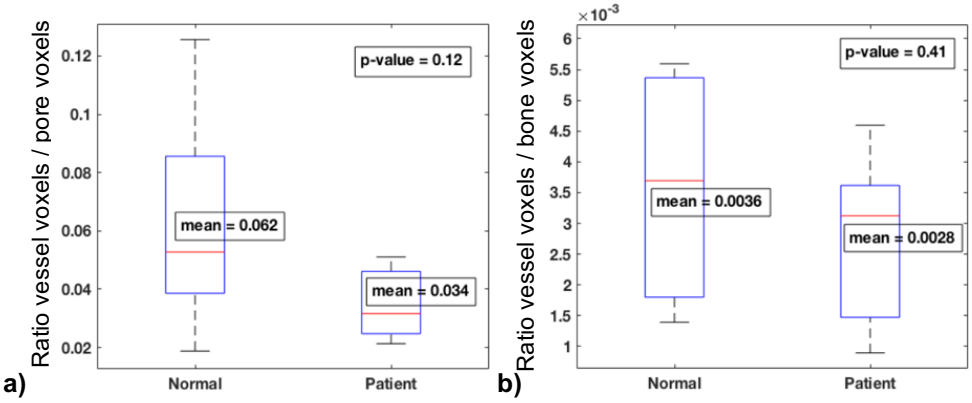


**Fig 10:** Comparison of blood vessel fractions between normal subjects and patients a) ratio of overlapped vessel voxels / pore voxels and b) ratio of overlapped vessel voxels / bone voxels

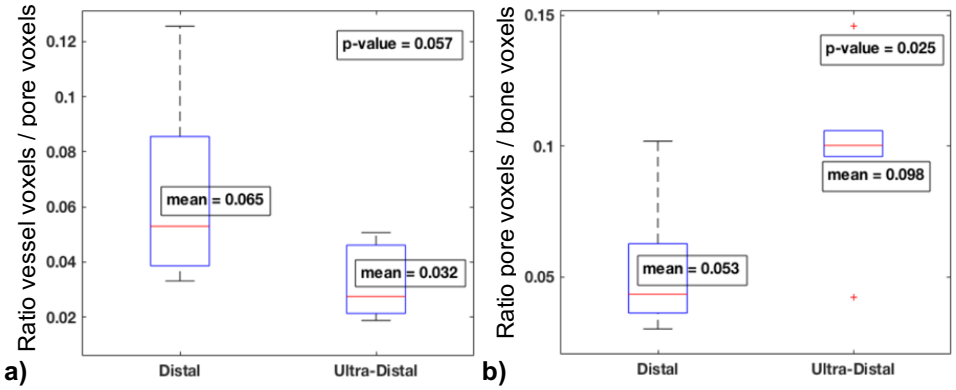


**Fig 11:** Comparison of vessel and pore voxels between the distal and ultra-distal tibia a) ratio of overlapped vessel voxels / pore voxels and b) ratio of pore voxels / bone voxels

Bone Mineral Density (BMD) was assigned to each voxel based upon the attenuation coefficient determined from the CT reconstructed image. The tibia data set exhibited several trends related to the voxel type (bone, blood vessel not overlapped with pore, pore, or blood vessel overlapped with pore). A comparison of the types based on the means for each data set is shown in Fig 12. As expected, the BMD decreased from highest in bone voxels to lowest in vessels voxels that overlap pore voxels. The difference between the means of each type was statistically significant with the largest p-value = 0.0057 for bone compared to the non-overlay vessel voxels. Whether vessel voxels were overlapped with pores or not, their BMD was less than the mean pore or bone voxel, respectively. This indicates that vessel voxels tend to be identified in volumes of lower BMD. This is reasonable since all true vessels should reside in pores. Differences also existed between the distal and ultra-distal tibia with the ultra-distal having a consistently lower BMD for bone (distal = 888 mg HA/ccm, ultra-distal = 832 mg HA/ccm, p-value = 0.0023) and for vessels that overlap pores (distal = 379 mg HA/ccm, ultra-distal = 330 mg HA/ccm, p-value = 0.091).

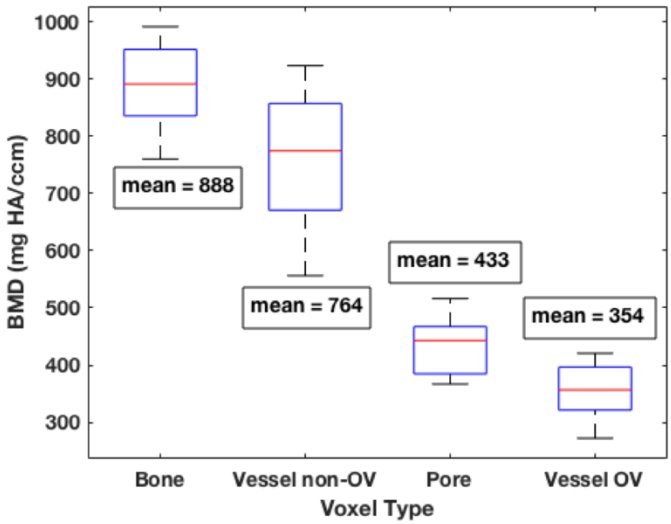


**Fig 12 :** Comparison of BMD for the voxels types: bone, non-overlap vessels, pores, and overlap vessels

### 3.4 Numerical phantom

The numerical phantom was used to characterize pipeline 2 and determine the impact on the vessel mask and the registration of vessels to pores. A measure of the impact was given by comparing the number of vessel voxels before and after registration. A measure of the alignment was given by the dice coefficient for vessel to pore overlap. For each response two factors were considered: the initial offset between the vessel and pore masks and the volume fraction of pores in the cortical bone. The results for the numerical phantom are shown in Fig 13. For each response, the data is plotted as a function of displacement in units of voxels. The vessels were rotated from $0^{o}$ to $18^{o}$ which for the 85-voxel radius resulted in a 0 to 27 voxel shift along the circumference. This rotational displacement appears to be a more strenuous test of the pipeline. Translations of the phantom led to less error in the final result.

The impact to the vessel mask is shown in Fig 13a as the total number of voxels in the vessels before and after the non-rigid registration of the MRI bone mask to the CT bone mask. Before non-rigid registration the rotation of the vessel configuration had very little effect on the vessel number (blue). Small fluctuations exist because of some deformation as the vessels were rotated and interpolated onto the image grid. The voxel counts after registration should be compared to the 8300 voxels expected (purple line) for the reduction of 10% in diameter (17% in vessel mask area). The non-rigid registration resulted in ~8% additional voxels for small displacements and near the correct number of voxels for large displacements. The additional voxels resulted when the MRI vessel position intersected the CT pore

position during the non-rigid registration. The registration appears to set the size of the vessel to the size of the pore when they were coincident. For large rotation displacements, the vessels do not intersect the pores during the non-rigid registration so they decreased in area consistent with the overall cortical bone. The root cause is confirmed by the result (red dashed) where vessels and pores were not included in the cortical bone masks. With the solid cortical bone masks, the voxel count remained near the expected value for all displacements.

The effect of registration of vessel to pores during image pipeline 2 is shown in Fig. 13b. The Dice coefficient is plotted as a function of displacement (voxels) and pore volume fraction (n). Here an ideal Dice coefficient was calculated:

$$DICE_{ideal} = 2\,(MRI \cap CT)/(MRI\ vessels\ ideal + CT\ vessels\ ) \quad (4)$$

where CT vessels = 10000 and the expected number of MRI vessels = 8300. Standard practice would be to normalize by the actual number of MRI vessels present in the processed image. However, the vessel number was reduced for larger offsets. Use of the expected number, provided an estimate of the MRI vessel deviation from the ideal. Each curve resulted from a different pore volume fraction where pore volume fraction was the number of pore voxels divided by the total number of voxels within the cortical bone boundary.

Two effects are evident in the data. For a displacement > 12 voxels or rotation > $10^{o}$, the accuracy falls off precipitously. Since the piecewise registration had a gradient based error metric, this was expected. Given large enough separation, there was insufficient intensity information to link the vessel location in the CT image to the vessel locations in the MRI image. The second effect was caused as pore volume fraction increased. A high pore volume fraction was equivalent to increased noise in the error surface of MRI to CT vessel alignment. Reduced contrast allowed the algorithm to reach a local minimum in the pore configuration without achieving proper alignment to the correct vessel / pore locations.

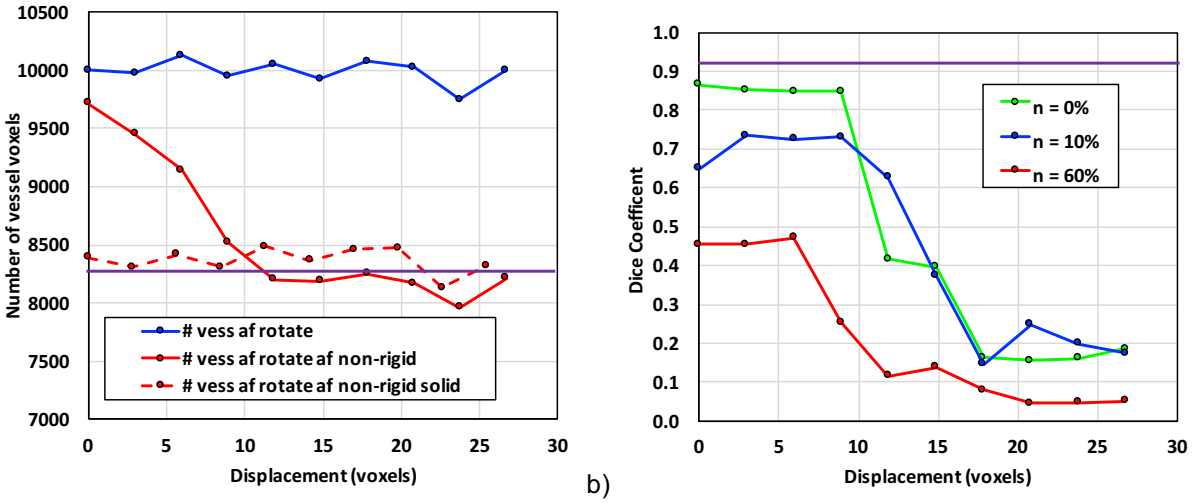


**Fig 13:** Numerical phantom results a) vessel voxels remaining after non-rigid registration and b) Dice coefficient impacted by displacement (voxels) and pore volume fraction (n).

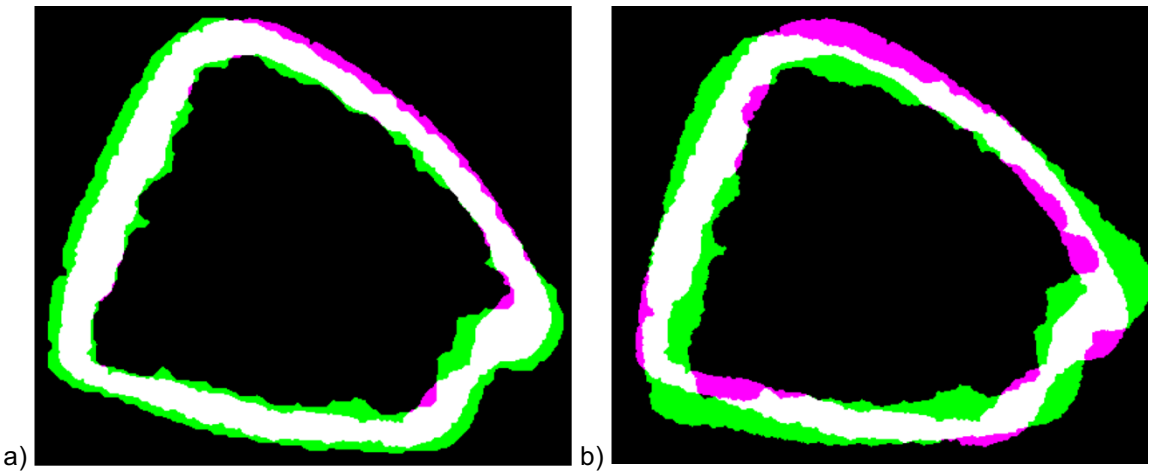


**Fig 14:** Cortical bone mask comparison of MRI and CT a) original rigid registration result and b) $10^{o}$ rotation of MRI

Distal tibia data sets should remain within the displacement limits for the algorithm. An example of the rigid registered MRI and CT cortical bone masks from data set prep008 UD are shown in Fig 14a. The cortical bone thickness was usually 30 voxels or less. It is unlikely for there to be a translation error in the registration of more than 1/3 the thickness. Fig 14b shows the MRI image purposely rotated $10^{o}$ with respect to the CT image. Such a gross misalignment is unlikely to exist after the rigid registration.

### 3.5 Physical Phantom

Results are divided into categories of voxel size calibration between the modalities, enhancement

features, and the image analysis pipeline for blood vessels.

Voxel size: The large phantom hole diameters are shown in table 3. They were measured using the ImageJ ROI tool [29]. The reported voxel sizes for MRI (230 μm) and CT (82 μm) were used to convert voxel into physical measurements.

**Table 3:** Comparison of large phantom hole diameters by modality

| Hole | DCE MRI (mm) | HR-pQCT (mm) | NU4 Spec (mm) | CT - MRI (um) | CT - MRI (CT voxel) | CT - MRI (%) |
|---|---|---|---|---|---|---|
| 1 | 0.899 | 1.083 | 1 | 184.2 | 2.25 | 17.0 |
| 2 | 2.174 | 2.150 | 2 | -23.5 | -0.29 | -1.1 |
| 3 | 3.138 | 3.154 | 3 | 15.8 | 0.19 | 0.5 |
| 4 | 4.152 | 4.223 | 4 | 71.9 | 0.88 | 1.7 |
| 5 | 4.968 | 5.039 | 5 | 70.9 | 0.86 | 1.4 |

The small phantom dimensions (channel and outer cylinder diameters) are shown in table 4. Results from the HR-pQCT and the MILabs VECTor4 spec are compared [30]. The holes were too close to the voxel size of the MRI to get consistent measurements. The channels with < 300 um diameter did not have consistent size in the HR-pQCT images.

**Table 4:** Comparison of small phantom hole diameters by CT

| Feature | HR-pQCT (mm) | VECTor4 Spec (mm) | Difference (μm) | Difference (%) |
|---|---|---|---|---|
| Hole 1 | 0.517 | 0.50 | -17 | -3.4 |
| Hole 2 | 0.424 | 0.40 | -24 | -6.0 |
| Hole 3 | 0.263 | 0.35 | 37 | 12.3 |
| Inner cylinder | 9.9 | 9.88 | -1 | 0.0 |
| Mid cylinder | 11.9 | 12.0 | 147 | 1.2 |
| Outer cylinder | 20.1 | 20.0 | -90 | -0.4 |

Enhancement features: Images of the large and small phantoms are shown in Fig 15. The contrast enhancement appears uniform for the channels of the large phantom in Fig 15a. The water surrounding the phantom has a lighter contrast than the dark PMMA of the phantom walls reminiscent of tissue to bone contrast. At the bottom of the image the dark boundary with air is visible. The HR-pQCT image in Fig 15b shows the high attenuation in the PMMA walls of the small phantom. The smallest hot

spot channels are not clearly visible. The small phantom MRI images are from the first and second MRI scans. It is encouraging that enhancement is visible in the smallest channels for the first MRI data set. However, the intensity is reduced and the spots are blurred together. These characteristics can affect vessel identification. Again, the smallest hot spot channels are not visible in the second scan. With residual water in the channels, the contrast agent would be excluded. The hot spot cylinder was also rotated from the 1$^{st}$ to the 2$^{nd}$ scan. Rotation occurred because the cylinder must be removed to change out the contrast solution, and orientation cannot be controlled when replacing the cylinder.

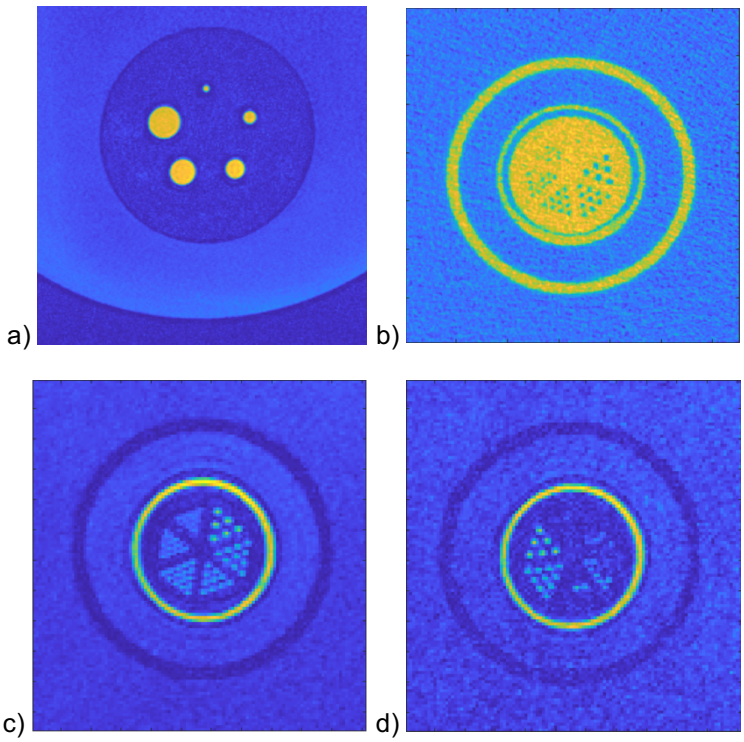


**Fig 15:** Phantom MRI images with contrast agent a) large phantom showing water container around phantom, b) HR-pQCT image of small phantom, c) first MRI acquisition of small phantom, and d) second MRI acquisition of small phantom

Fig 16 has histogram plots of the MRI voxel intensities in and around the large phantom. The peak at the lowest intensity is from PMMA followed by the peak for water. The peak at highest intensity is from the contrast enhanced channels. The differences between the first and second scans are significant. The absolute values and the relative positions of the PMMA and water peaks have substantially changed. The two peaks have partially merged in the second acquisition. For the data to be useable in creating a

pseudo-enhancement curve, the intensity distributions had to be adjusted so the PMMA and water regions cancelled between the two scans. Average intensities were calculated over volumes in the PMMA and water from the 1st and 2nd data sets. The linear fit was determined to match mean PMMA and water intensities in the 2nd acquisition to the first acquisition. The linear fit was then applied to the all intensities in the 2nd acquisition. The difference between the 1st acquisition and the scaled 2nd acquisition became the enhancement image where PMMA and water signals had cancelled.

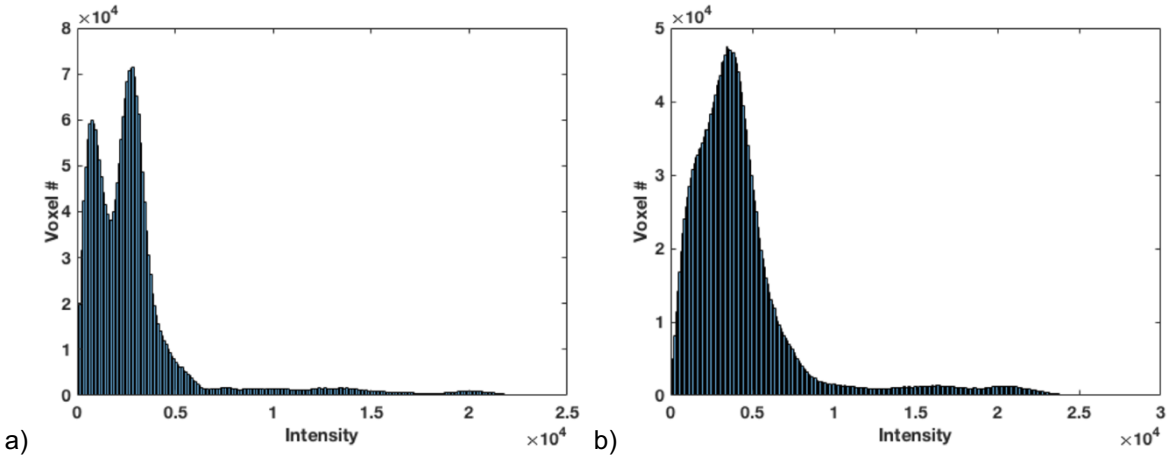


**Fig 16:** Intensity histograms for the MRI data from a) 1st scan and b) 2nd scan

A different procedure was used for the small phantom since there was inconsistent or no enhancement in the small channels. Scaling was not sufficient to create a useful data set. In this case a pseudo-enhancement data set was created by scaling the 1st acquisition by 120%. Only high intensity voxels were scaled by using a mask that blocked the low intensity voxels for PMMA and water in the scaling step. The difference between the pseudo-enhanced data and the original data provided the enhancement data for the small phantom.

The resulting enhancement curves are plotted in Fig 17. The data for each is from a single voxel to highlight the variation between the 18 acquisitions over time. Plots are from the 5 mm, 500 μm, and 220 μm channels. Of course, this is a best-case indicator since there were no effects from patient motion or blood flow. The larger channels had variation that was much smaller than the enhancement with standard deviation ~1% of the mean intensity. The variation for the small channel was ~5% of the mean intensity which was significant compared to the pseudo-enhancement magnitude. The larger variance

arose from a washout like trend in the data; however, there was no washout in the static phantom.

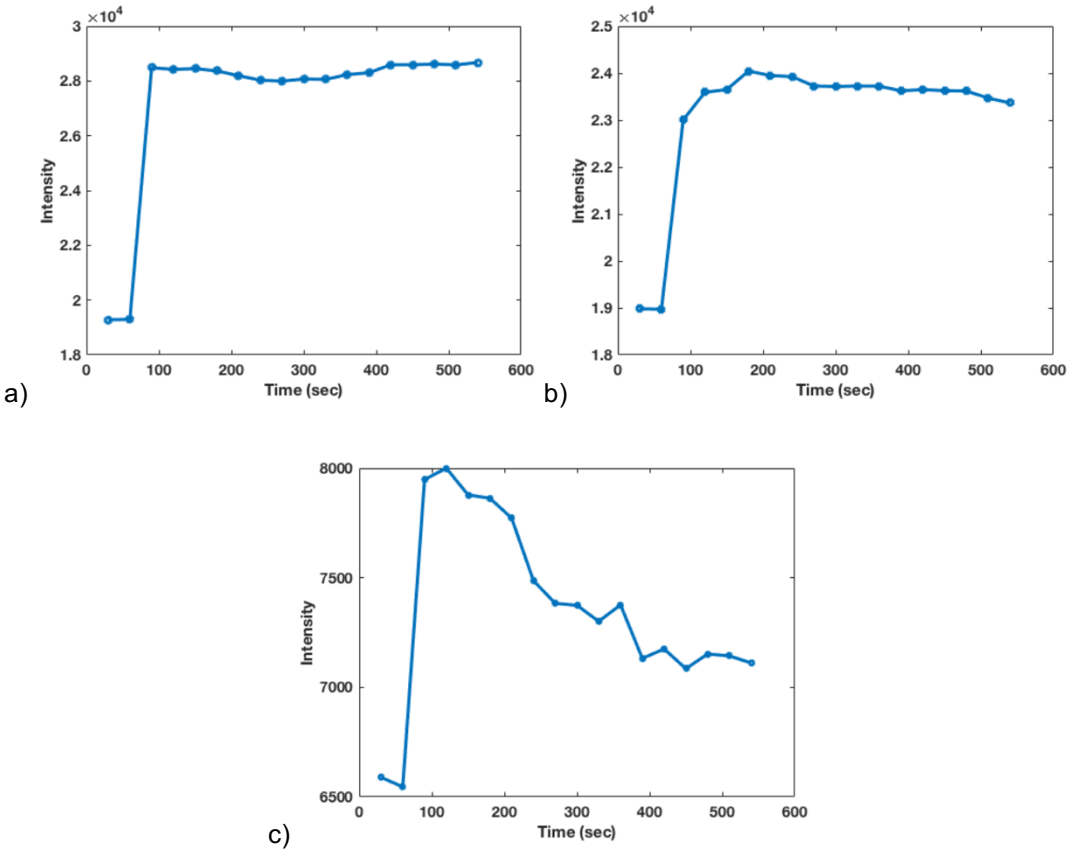


**Fig 17:** Enhancement curves for a) large phantom (5 mm channel), b) small phantom (500 μm channel), and c) small phantom (220 μm channel)

Image analysis pipeline: Processing the phantom data through the image pipeline provided insight into generation of the vessel masks and ability to align vessels with pores for objects where the ground truth was known. Figs 18 and 19 are 3D visualizations of the vessel masks for the large and small phantoms.

With the large phantom, the range of Frangi scale factors required adjustment to larger values for correct identification of the channels with large diameter. Instead of the few 100 μm diameters of blood vessels in cortical bone, the channels reach a diameter of 5 μm. Erroneous vessel voxels may be generated when the Frangi scale range does not encompass the range of actual vessels. Another interesting feature of these vessel masks was the presence of voxels identified as vessels throughout the volume of the non-enhanced PMMA. The density of spurious vessels was low when the large channels were correctly defined (Fig 18a large Frangi scale factors), but high when only remnants of the large

channels existed (Fig 18b small Frangi scale factors).

a) 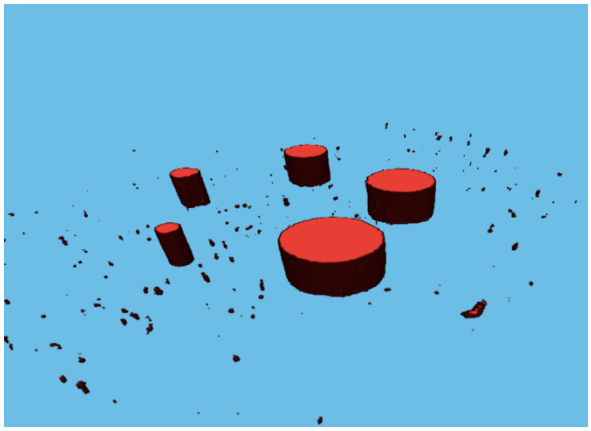 b) 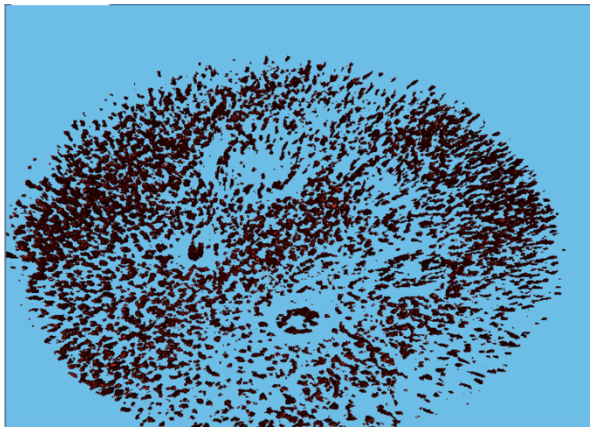

**Fig 18:** Vessel masks from the large phantom with Frangi scale range a) 2 to 10 and b) 0.75 to 1.25

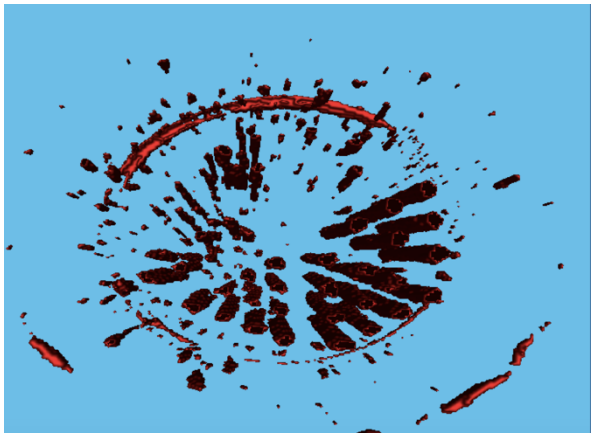

**Fig 19:** Vessel mask from the small phantom with Frangi scale range 0.25 to 3.25

Metrics from the vessel alignment pipeline are listed in table 5. Since the cortical bone mask was a simple cylinder, the registration algorithms produced a close match between CT and MRI mask with Dice coefficients of 0.985. The overlap of vessels with pores reached 100%, and the overlap of vessel voxels with pore voxels was also high (96% large channels and 81% small channels).

There are discrepancies between the number of segmented vessels reported in table 5 vs the actual number of channels. Extra vessels existed because of the erroneous vessel voxels described above. As seen in fig 18 and 19, the erroneous vessels were smaller than the actual channels; however, they still affected the vessel calculations of table 5. In the large phantom, the final number of vessels reported was 15 while only 5 channels exist in the phantom. It was observed that the 5 large channels

were properly identified and aligned as part of the 15 vessels reported.

The small phantom indicates the size of channels that can be resolved. The channel arrays are mostly intact down to the 300 μm size as shown in Fig 19. Below that size only fragments of the channels remained. Nonetheless, the piecewise rigid registration algorithm was able to achieve the final alignment of the vessel and pore arrays. This is shown in Fig 20 which has before and after images of the overlapped masks. The separation of the purple (vessel) and green (pore) channels are visible in the before image. The channels have become aligned (white) in the after image. The large green annulus is the pore mask (open space) between the concentric tubes of phantom walls.

**Table 5:** Characteristics of the bone masks and overlap of vessels from the alignment pipeline

| Phantom | Dice: cortical bone mask | | % overlap: voxels | | % overlap: vessels | | Number of vessels | | Number of Channels |
|---|---|---|---|---|---|---|---|---|---|
| | Af global rigid | Af non-rigid | Initial | Final | Initial | Final | Initial | Final | Actual |
| Large | 0.973 | 0.985 | 68.6% | 96.3% | 1.96% | 100% | 204 | 15 | 5 |
| Small | 0.966 | 0.985 | 35.4% | 80.7% | 63.0% | 100% | 235 | 61 | 66 |

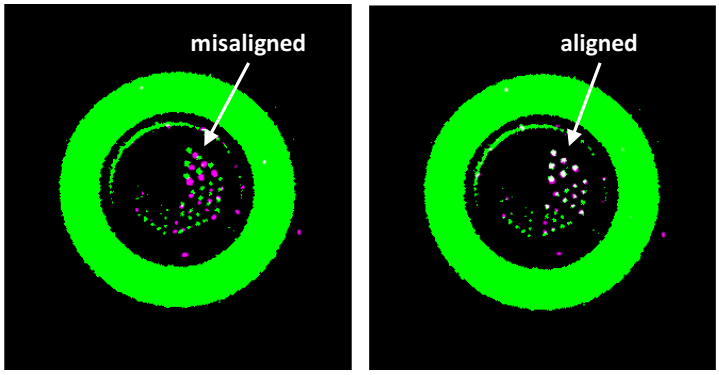


**Fig 20:** Combined images of the vessel and pores masks a) before and b) after piecewise registration

The smaller, more densely packed arrays suffered from both a reduction in signal and the overlap of signal between nearest neighbors. Instead of individual channels, the intensity became more uniform across the whole volume of the array. Table 5 does not indicate which of the actual 66 channels are represented in the final number of vessels reported. Table 6 provides an additional measure to quantify the capability of pipeline 2. The ratio was taken of the VECTor4 total channel volume (ground truth) [30] in

each array to the volume measured from the vessel mask. The fraction dropped from 1.0 for the 500 μm array to 0.091 for the 220 μm array.

**Table 6:** Vessel mask volume within each channel array type

| Array type | Channel Diameter Spec (μm) | # of channels | Total volume (μm3) | Fine resolution volume (voxels) | Vessel mask volume (voxels) | Volume Fraction |
|---|---|---|---|---|---|---|
| 1 | 500 | 6 | 71.7e6 | 10666 | 10691 | 1.00 |
| 2 | 400 | 10 | 76.7e6 | 11400 | 6761 | 0.59 |
| 3 | 350 | 10 | 58.7e6 | 8728 | 2445 | 0.28 |
| 4 | 300 | 10 | 43.1e6 | 6413 | 1035 | 0.16 |
| 5 | 250 | 15 | 44.9e6 | 6680 | 835 | 0.13 |
| 6 | 220 | 15 | 34.8e6 | 5173 | 473 | 0.091 |

### 3.6 MRI Reproducibility

The prep008 ultra-distal data set was investigated for reproducibility by separating alternating time points. The blood vessel networks derived from the MRI data are compared as 3D renderings in Fig 21. The first image is the network resulting from the full data set. Fig 21b illustrates the voxels remaining after subtraction of the odd data set from the even data set before processing through pipeline 2. A scattering of voxels remains due to differences in shape and alignment between the data sets. Fig 21c is the combination of the even data network before and after pipeline 2. The displacement is sufficient to completely separate the vessels. Fig 21d is the subtraction of the odd and even data sets after they were separately processed through pipeline 2. The scattering of residual voxels is denser than the result from the initial images. The pipeline did not move the networks to exactly the same location, but it was close. Differences between the two vessel networks and multiple minima allowed by the error surface for pore alignment allows convergence to slightly different locations.

Table 7 compares characteristics of the vessel and pore networks. The fraction of overlap with pores for segmented vessels as well as vessel voxels was effectively the same for the three cases. The difference became significant only for the absolute size of the vessel network. The full data set had ~10% larger vessel volume which did affect the biomarker value of vessel to pore volume fraction. The relative variability between separate full data sets was estimated by comparing the even and odd data sets here. The differences in vessel number and volume fraction were < 2%.

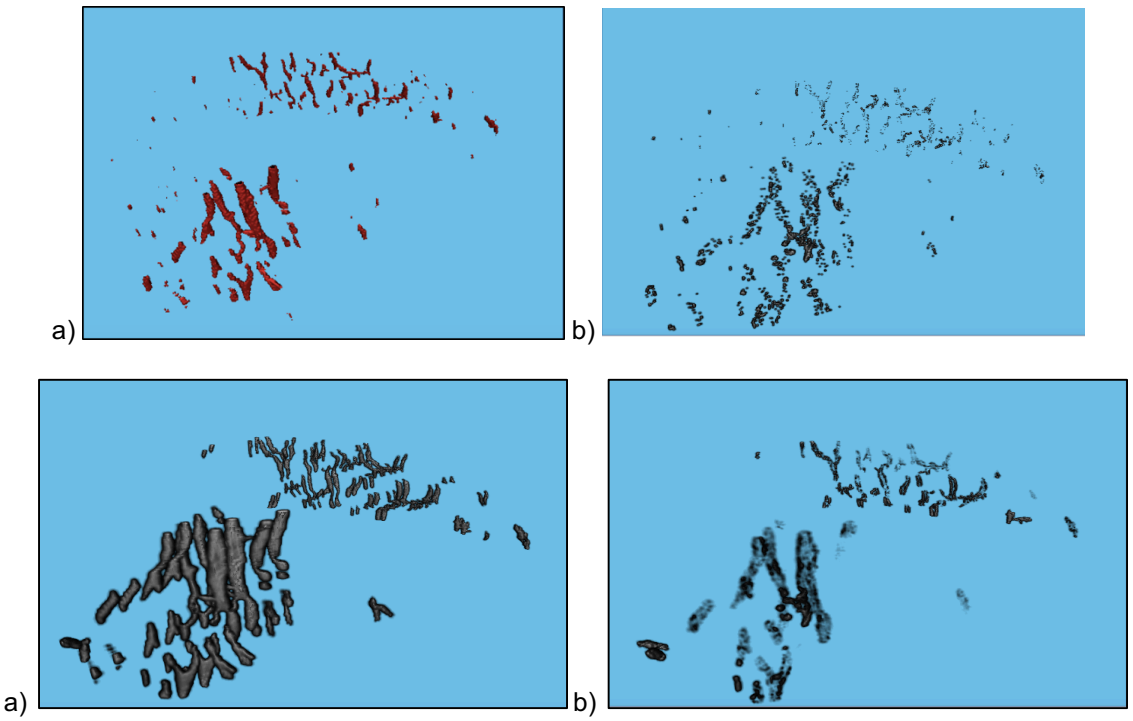


**Fig 21:** Comparisons of the blood vessel networks a) Original full data set network, b) Subtraction of odd and even networks, c) Even network before and after the alignment pipeline, and d) Subtraction of odd and even networks after the alignment pipeline.

**Table 7:** Comparison of characteristics for the vessel networks from separated data sets

| Characteristic | Full | Even | Odd | Diff odd/even | Diff full/even |
|---|---|---|---|---|---|
| Vessels | 35 | 32 | 32 | 0.00% | 8.57% |
| Vessel voxels | 12320 | 11008 | 10826 | 1.68% | 10.65% |
| Pore voxels | 275262 | 274364 | 274289 | 0.03% | 0.33% |
| Overlap vessel fraction | 0.897 | 0.889 | 0.889 | 0.00% | 0.95% |
| Overlap vessel voxel fraction | 0.863 | 0.865 | 0.870 | -0.56% | -0.21% |
| Overlap vessels / pores | 4.48% | 4.01% | 3.95% | 1.52% | 10.49% |

**Table 8:** Dice coefficients for overlap of blood vessel networks

| Compare | Data type | Dice |
|---|---|---|
| even / odd | before pipeline | 0.896 |
| even / odd | after pipeline | 0.631 |
| full / even | after pipeline | 0.630 |

The overlap and similarity of these blood vessel networks was quantified with the Dice coefficient. As initially generated, the even and odd vessel networks were almost the same size (table 8) and overlap with Dice ~ 0.90. After processing through the image pipeline for pore alignment, the Dice

coefficients dropped to ~ 0.63.

Tables 9 and 10 summarize biomarkers of vessel volume fraction defined as the normalized vessel area (mm2/mm2) and normalized vessel number (#/mm2). They were normalized by the cortical bone area in each CT slice and for each lamina (endosteal, mid-cortical, periosteal). The values reported were the average over all slices. As shown above, the full data set identified a larger volume of voxels as blood vessels. The even and odd data sets were relatively consistent with differences of ~2% or less in the mid-cortical and periostel lamina. The larger differences in the endosteal lamina were due to statistical fluctuations given the small number of vessels in that lamina.

**Table 9:** Normalized blood vessel area (mm2/mm2)

| Lamina | Full | Even | Odd | Diff full/even | Diff even/odd |
|---|---|---|---|---|---|
| endosteal | 0.075% | 0.057% | 0.051% | 31.8% | 10.6% |
| mid-cortical | 0.728% | 0.672% | 0.662% | 8.3% | 1.57% |
| periosteal | 2.20% | 2.03% | 2.03% | 8.4% | 0.30% |

**Table 10:** Normalized vessel number (#/mm2)

| Lamina | Full | Even | Odd | Diff full/even | Diff even/odd |
|---|---|---|---|---|---|
| endosteal | 0.0081% | 0.0055% | 0.0059% | 47.21% | -5.95% |
| mid-cortical | 0.0518% | 0.0437% | 0.0444% | 18.44% | -1.44% |
| periosteal | 0.1850% | 0.1684% | 0.1648% | 9.85% | 2.16% |

## 4 DISCUSSION and CONCLUSION

In this project, routines were developed to cross check masks of cortical bone, blood vessels and pores; to identify overlap between blood vessels and pores; and to report characteristics of the resulting blood vessel networks. These capabilities will assist in researching disease effects on the mechanisms driving pathological bone porosity.

### 4.1 Bone data sets

The routines for the MRI bone mask created boundaries that were generally consistent under visual inspection of the MRI raw data. However, the MRI boundaries were not always coincident with the boundaries of the CT bone mask. Discrepancies between the shapes of the CT and MRI bone appeared to be the cause. The rigid registration of the CT to the MRI from image pipeline 1 appears to have been

effective so the discrepancies were not caused by the mask generation routines. They were discrepancies in the MRI images. This conclusion was arrived at because pores in the MRI data are distorted along with the bone boundaries. The pore patterns in the MRI data were correlated but not coincident to similar pore patterns in the CT data.

Artifacts in the MRI may be a cause for differences between masks. One effect could be MRI chemical shift, $\Delta x_{CS}$ [31]. Normalizing by the MRI resolution, we find

$$\Delta x_{CS}/\delta x = f_{CS} N_{FE}/(2 \cdot BW) = (440\ Hz \cdot 512)/(2 \cdot 125\ kHz) = 0.9 \quad (5)$$

where $f_{CS} = \text{chemical shift}$, $N_{FE} = \text{number of FE}$, and $BW = \text{half bandwidth}$. Since the MRI resolution was 3x worse than the CT resolution, there was a chemical shift effect of ~3 pixels in the CT domain. This was noticeable, but not large enough to explain the discrepancies between the masks. Another artifact of potential concern would be pile-up and stretch artifacts due to magnetic susceptibility differences with the Gd and bone [32]. Higher intensity from enhancement, encroaching into the cortical bone and deformation of bone, was visible in some data sets.

While the mentioned effects may impact the shape of the MRI bone, more work is required to determinate the root causes for the shape anomalies. A diagnostic for this issue would be a scan with a MRI sequence having different contrast. The patient scan protocol includes a MRI FIESTA-C sequence [33]. At present, the sequence implemented has low SNR. It may be useful to adjust the FIESTA scan parameters for higher SNR since the images are too noisy for diagnostic purposes. The FIESTA results could then be compared to SPGR for more insight with respect to resolution and bone boundary locations.

The non-rigid registration of the routines was sufficient to morph the shape of the MRI bone into that of the CT bone, increasing Dice coefficients from ~0.8 to ~0.9. The deformation moved the blood vessels embedded within the MRI bone mask closer to pores embedded within the CT bone mask. The improvement was evident in the increased vessel to pore overlap fraction. However, some deformation of the vessels themselves occurred. The amount of deformation may be affected by the inclusion of pores in the CT and MRI bone masks used for the non-rigid registration. The algorithm attempted to morph pores in the MRI mask toward the shape of pores in the CT mask. The impact was small since the pore distributions do not change much, but the effect may be non-negligible. To investigate this, follow-on work

for the non-rigid registration should include testing different versions of the bone masks. The mask versions to test are: no pores, filled trabecular compartment, and no pores with filled trabecular compartment.

The final step with piecewise rigid registration resulted in significant improvement in pore alignment. This was indicated by the increase in overlap fractions to ~40% of vessel voxels and ~90% of vessels themselves. These numbers quantified the qualitative conclusion from the visual inspections that the overlapped voxels defined contiguous blood vessels while the overlapped pores acted as an envelope to decrease the blood vessel extent.

Uncertainty remains as to correct matching of specific vessels to pores. Fortunately, the results indicate areas to pursue in order to increase algorithm robustness. One area, high pore volume fraction, could make proper alignment difficult. However, data sets with low overlap fraction data do not have a higher pore volume fraction than data sets with high overlap fraction. This indicates that pore volume fraction is probably not a contributing factor. To ensure no adverse impact, additional analysis should be done to quantify whether local volumes of high pore volume fraction exist around any blood vessels. A second concern relates to data sets with lower overlap fraction that have high vessel densities combined with small mean vessel size. While this relationship may have a biological basis, it may also result from the vessel identification pipeline. Image noise, registration errors, and other sources will cause a certain enhancement noise signal to exist in voxels. If large enough, some voxels will be placed in the k-means group designated as vessels. The issue will be exacerbated if the real vessels in a sample have low enhancement signal. The fact that data sets with smaller mean vessel size have both worse overlap and more vessels far from any pores may be an indicator of this problem. Improvements should be investigated by adjusting the Frangi method parameters, the k-means features, or other steps in the vessel identification pipeline 1. The phantom test results can provide guidance in this effort. Another avenue to improve registration is in the VOI definition for the piecewise rigid method. At present, the algorithm allows user input of the dilation parameter to determine VOI size, but the same dilation is applied across the entire image volume. An automated algorithm that adjusts across the volume and has dependence on local conditions could improve the VOI sizes for local registration.

These algorithm improvements along with analysis of more data sets will be needed to ascertain whether there are statistically significant differences in vessel densities between populations. The T2D study itself is only in initial stages with few subjects. Nonetheless, the available results provide useful feedback for improvements of the image analysis pipeline. The limited data sets so far have vessel densities in bone of 3.6% normal and 2.8% T2D with p-value = 0.41. Nonetheless, there are some trends of note in the data. As expected, the mean BMD of vessel voxels is less than that of bone voxels by more than a factor of 2. The vessels voxels, after the alignment pipeline, also exhibit a lower mean BMD than the pore voxels. This is possible since the vessels should reside within the envelope of the pores. Higher pore volume fraction is observed in the ultra-distal tibia while the blood vessel volume fraction is approximately the same in distal and ultra-distal tibia.

### 4.2 Numerical phantom

The numerical phantom analysis provides useful metrics for bone and vessel data sets to determine whether the image pipeline with return robust results. Inspection of pore and vessel locations within the cortical bone indicates whether the networks meet the metric of being <15 voxels from each other. As part of such inspections, rotational displacements could be more of a detriment than translational. Pore densities as a fraction of the cortical bone volume < 20% are at lower risk for error in the vessel alignment. These metrics were determined in the numerical phantom with simple arrays of columns. The image pipeline may be capable for larger displacements or pore densities with actual blood vessel networks. This is because the columns used for the phantom do not have the complex, 3-D extent that would expand the volume where moving and fixed images have overlap of intensity patterns. Complex, connected shapes may also stand out better against a noisy pore background. Next steps in this research should include realistic vessel networks in the phantom. One method for creation of artificial blood vessel networks was reported by Van Leeuwenn, et. al. [34].

### 4.3 Physical phantom

The phantom data has confirmed the calibration of the voxel size for MRI relative to CT. The large phantom channels had small, sub-voxel differences which validates the reported sizes. The larger error in the smallest hole results may be due to manual ROI tool placement instead of intrinsic to the modalities. This indicates that voxel size is not the cause of discrepancies between the MRI bone mask and the CT

bone mask. The vessel alignment pipeline has shown itself capable to align vessels with pores having dimensions down to 300 μm. The algorithm may be capable to smaller dimensions as long as the provided vessel mask is correct. With this phantom data, the vessel mask did not replicate the arrays below channel diameters of 300 μm. However, this is a worst-case test for the vessel identification algorithm. The falloff may not be as severe for isolated features as it is for these close packed arrays.

Lack of signal in the smallest channels of the 2nd MRI scan and presence of attenuation in the CT scan, indicated that residual water was present in the smallest channels. Note that PMMA and water have similar x-ray attenuation [35]. Water was used to extract the hot spot cylinder from the inner phantom cylinder after the MRI scan. The hot spot cylinder was dried, but apparently not enough to evacuate the smallest channels. To complete these measurements, a follow-up HR-pQCT scan should be completed after confirmation that all liquid has evaporated.

The creation of erroneous vessel voxels in the PMMA walls of the large phantoms was similar to patient data sets that exhibit vessel voxels far from pore voxels in the cortical bone. The characteristics of those voxels may indicate root causes. The number of erroneous voxels greatly increased for the case where the Frangi scale factors excluded most voxels in the large channels of the large phantom. This reduced the signal of channel voxels relative to the noise floor. If the signal from actual vessel voxels was not sufficiently above the noise, the algorithm may have identified as vessels those voxels in non-enhancing volumes that have large noise.

Several next steps are indicated by these phantom experiments. If scan time can be procured, it would be beneficial to run the MRI scan again using the same prescan calibration for both contrast concentrations. Then the difference between two enhancement data sets could be taken with consistent contrast for all materials. The second MRI scan as well as an additional HR-pQCT scan should be performed after ensuring the small channel arrays are completely dry. This data will be needed to further analyze the alignment capability for small channels. Investigation is needed to understand the generation of erroneous vessels evident in the large phantom data, and the loss of small vessels evident in the small phantom data. These conditions effect the function of the Frangi vessel algorithm and the partition into groups by k-means. Actions include alternate selection of scale factors and use of different features for k-means. These modifications to the image pipeline can be tested on the phantom data to determine

whether erroneous vessel voxels are eliminated and correct vessel voxels are increased as functions of vessel size and intensity. Characteristics of the phantom data such as noise and point spread function, derived from the physical phantom data, can be incorporated into numerical phantom experiments to improve predictability. Finally, the root cause for the washout like behavior in the enhancement signal for small channels deserves further investigation, to determine whether it is a significant noise contributor in patient scans.

### 4.4 MRI Reproducibility

The small difference in vessel quantities (~2%) between the even and odd data sets provides confidence that derived quantities are reproducible. It is an indicator that repeated scans using the same data set protocol will report similar biomarker values such as overall vessel volume fraction. Of concern is the difference between the down selected data sets (9 time points) vs the full data set (18 time points). The alternating data sets may exhibit different variability for several parameters than would several full data sets. There should be similar impact from patient motion since similar variability will occur between any set of time points. This analysis may highlight differences due to longitudinal acquisitions at variable points along the enhancement curve. In practice, variation in timing between Gd injection, wash-in, scan start, heart rate, vasodilation, and other physiological variations will cause differences between separate scans of the same patient. The shape of the enhancement curve has an effect on blood vessel identification, and alternate time points will change the shape. The magnitude of the mentioned effects may be larger compared to a standard data set. Nonetheless, this analysis should provide insight as a worse case estimate into repeatability effects. At some number of time points the local vessel properties should asymptote, but additional analysis would be required to determine that number.

Local differences on the scale of the blood vessel widths can be significant as indicated by Dice coefficients (~0.63) comparing the even and odd data sets after the alignment pipeline. Recall that before alignment the slight differences between the even and odd vessel masks resulted in a Dice coefficient of 0.9. This implies a pipeline 2 related effect of Dice ~ 0.7. The pipeline 2 impact is due to a combination of voxel changes from grid interpolation during registration and slight differences in final vessel locations after alignment. As an example, a typical blood vessel has a diameter of ~5 voxels. An offset of 1.5 voxels would reduce the Dice coefficient to 0.7. A misalignment of 1.5 voxels on the CT grid is ~ ½ voxel

misalignment on the MRI grid where the MRI CE data originates. Given the consistency of the global biomarker values, the observed Dice coefficients with sub-voxel alignments on the MRI grid may be acceptable. Additionally, the algorithm improvement actions listed in the previous sections should mitigate these local discrepancies.

### 4.5 Conclusion

In this project, routines were developed to cross check masks of cortical bone, blood vessels and pores; to identify overlap between blood vessels and pores; and to report characteristics of the resulting blood vessel networks. After registration, the MRI bone masks are aligned with the CT bone masks. While the impact of MRI artifacts is mitigated by the image pipeline, further investigation is needed to ensure no effect on reported blood vessel characteristics.

The vessel to pore alignment pipeline can exhibit high alignment fractions for distal tibia and phantom data sets. This shows proof of concept for the general approach as well as the implemented algorithms. For some data sets alignment is not as high, and the phantom data indicates the creation of erroneous vessel voxels by the vessel mask image pipeline. The analysis of both bone and phantom data has led to the definition of metrics and identification of specific algorithm deficiencies. Future work on these items should result in a robust image analysis pipeline for most data sets and a set of useful metrics to distinguish problematic data sets for additional analysis.

**REFERENCES**

**[1]** Gentry SD, Bramblett CA. The Anatomy and Biology of the Human Skeleton. Texas A&M University Press. p. 4. ISBN 0-89096-300-2; 1988.

**[2]** Birbrair A, Frenette P. Niche heterogeneity in the bone marrow. *Annals of the New York Academy of Sciences*. 2016;1370(1):82–96. doi:10.1111/nyas.13016.

**[3]** Borderi M, Gibellinib D, Vescinic F, De Crignisb E, Cimattib L, Biagettia C, Tampellinia L, Re MC. Metabolic Bone Disease in HIV Infection. *AIDS*. 2009;23:1297–1310. doi:10.1097/QAD.0b013e32832ce85a.

**[4]** Choi YJ, Chung Y-S. Type 2 diabetes mellitus and bone fragility: Special focus on bone imaging. *Osteoporosis and Sarcopenia*. 2016;2:20–24. doi: 10.1016/j.afos.2016.02.001.

**[5]** Samelson EJ, Demissie S, Cupples LA, Zhang X, Xu H, Liu C-T, Boyd SK, McLean RR, Broe KE, Kiel DP, Bouxsein ML. Diabetes and Deficits in Cortical Bone Density, Microarchitecture, and Bone Size: Framingham HR-pQCT Study. *Journal of Bone and Mineral Research*. 2018;33(1):54–62. doi: 10.1002/jbmr.3240.

**[6]** Heilmeier U, Cheng K, Pasco C, Parrish R, Nirody J, Patsch JM, Zhang CA, Joseph GB, Burghardt J, Schwartz AV, Link TM, Kazakia G. Cortical bone laminar analysis reveals increased midcortical and periosteal porosity in type 2 diabetic postmenopausal women with history of fragility fractures compared to fracture-free diabetics. *Osteoporos Int*. 2016;27(9):2791-2802. doi: 10.1007/s00198-016-3614-7.

**[7]** Marenzana M, Arnett TR. The key role of the blood supply to bone. *Bone research*, 2013;1:203-215.

**[8]** Nishiyama KK, Shane E. Clinical Imaging of Bone Microarchitecture with HR-pQCT. *Curr Osteoporos Rep*. 2013;11(2):147–155. doi:10.1007/s11914-013-0142-7.

**[9]** Kroker A, Zhu Y, Manske SL, Barber R, Mohtadi N, Boyd SK. Quantitative in vivo assessment of bone microarchitecture in the human knee using HR-pQCT. *Bone* 2017;97:43-48. doi: 10.1016/j.bone.2016.12.015.

**[10]** Sourbron SP, Buckley DL. Classic models for dynamic contrast enhanced MRI. *NMR in Biomedicine*. 2013;26(8):1004–1027. doi: 10.1002/nbm.2940.

**[11]** Jackson A, O'Connor JPB, Parker GJM, Jayson GC. Imaging Tumor Vascular Heterogeneity and Angiogenesis using Dynamic Contrast-Enhanced Magnetic Resonance Imaging, *Clinical Cancer Research*, 2007;13(12):3449–3459. doi: 10.1158/1078-0432.CCR-07-0238.

**[12]** Kazakia, G., UCSF Radiology internal progress report, R03AR064004. 2017.

**[13]** Wu P, Liu J, Carballido-Gamio J, Han M, Krug R, Kazakia G. Cortical Bone Vessel identification on Contrast-Enhanced MR images, *JOINT ANNUAL MEETING ISMRM-ESMRMB*, Paris, France. 2018.

**[14]** Kazakia GJ, Tjong W, Nirody JA, Burghardt AJ, Carballido-Gamio J, Patsch JM, Link T, Feeley BT, Ma CB. The influence of disuse on bone microstructure and mechanics assessed by HR-pQCT. *Bone.* 2014;63:132–140.

**[15]** Jenkinson M, Beckmann CF, Behrens TE, Woolrich MW, Smith SM. Review FSL. *NeuroImage*, 2012;62:782–790.

**[16]** Buie HR, Campbell GM, Klinck RJ, MacNeil JA, Boyd SK. Automatic segmentation of cortical and trabecular compartments based on a dual threshold technique for in vivo micro-CT bone analysis. *Bone*. 2007;41(4):505-15.

**[17]** Burghardt AJ, Buie HR, Laib A, Majumdar S, Boyd SK. Reproducibility of direct quantitative measures of cortical bone microarchitecture of the distal radius and tibia by HR-pQCT. *Bone*. 2010;47(3):519-28. doi: 10.1016/j.bone.2010.05.034.

**[18]** Abdi H, Williams L. Principal Component Analysis. *WIREs Comp Stat* 2010;2:433–459.

**[19]** Frangi A, Niessen W, Vincken K, Viergever M. Multiscale vessel enhancement filtering, in [Medical Image Computing and Computer-Assisted Intervention – Miccai'98], Wells W, Colchester A, Delp S, eds., 1998;1496:130-137, Springer-Verlag Berline, Berlin.

**[20]** Jain AK. Data Clustering: 50 Years Beyond K-Means. *Pattern Recognition Letters*, 2010;31(8):651-666.

**[21]** Kerschnitzki M, Kollmannsberger P, Burghammer M, Duda GN, Weinkamer R, Wagermaier W, Fratzl P. Architecture of the osteocyte network correlates with bone material quality. *J. of Bone and Mineral Research*, 2013;28(8):1837-1845.

**[22]** MATLAB Release 2017a, The MathWorks, Inc., Natick, MA, USA; 2017.

**[23]** Thirion JP. Image matching as a diffusion process: an analogy with Maxwell's demons. *Medical*

*Image Analysis*, 1988;2(3):243–260.

**[24]** Zitova B, Flusser J. Image registration methods: a survey. *Image and Vision Comput*, 2003;21:977–1000.

**[25]** Specifications for Phantom QRM-MicroPET-IQ to meet NEMA standard NU 4-2008, QRM Quality Assurance in Radiology and Medicine GmbH, Baiersdorfer Str. 22, 91096 Moehrendorf, Germany, http://www.qrm.de/content/products/microct/micro-pet-iq.htm

**[26]** MILabs. User Manual: U-SPECT4, U-PET4, VECTor4," www.milabs.com, company manual.

**[27]** Wichlas, F, Bail JH, Seebauer CJ, Schilling R, Pflugmacher R, Pinkernelle J, Rump J, Streitparth F, Ulf Teichgraber KM. Development of a Signal-Inducing Bone Cement for Magnetic Resonance Imaging. *J. of Mag. Res. Imaging*, 2010;31:636–644.

**[28]** Kanal E, Maravilla K, Rowley HA. Gadolinium Contrast Agents for CNS Imaging: Current Concepts and Clinical Evidence, *American Journal of Neuroradiology*, 2014;35(12):2215-2226. DOI: doi: 10.3174/ajnr.A3917.

**[29]** Rueden CT, Schindelin J, Hiner MC, DeZonia BE, Walter AE, Arena ET, Eliceiri KW. ImageJ2: ImageJ for the next generation of scientific image data, *BMC Bioinformatics* 2017;18:529, doi: 10.1186/s12859-017-1934-z.

**[30]** Ivashchenko O, Van der Have F, Villena JL, Groen HC, Ramakers RM, Weinans HH, Beekman FJ. Quarter-Millimeter-Resolution Molecular Mouse Imaging with U-SPECT. Molecular Imaging. 2014;13:1–8.

**[31]** Nishimura DG, Principles of Magnetic Resonance Imaging. (1.2 ed). www.lulu.com; 2016.

**[32]** Hashemi RH, Bradley WG, Lisanti CJ. *MRI: The Basics.* (3rd ed). Philadelphia, PA: Lippincott Williams & Wilkins; 2010.

**[33]** Chavhan GB, Babyn PS, Jankharia BG, Cheng HM, Shroff M., Steady-State MR Imaging Sequences: Physics, Classification, and Clinical Applications. *RadioGraphics.* 2008;28(4):1147–1160. doi: 10.1148/rg.284075031.

**[34]** Van Leeuwenn G, Kotte A, Lagendijk J, A Flexible Algorithm for Construction of 3-D Vessel Networks for Use in Thermal Modeling, *IEEE Trans Biomed Eng*, 1998;45(5):596–604.

**[35]** ICRU (1989), *Tissue Substitutes in Radiation Dosimetry and Measurement,* Report 44 of the International Commission on Radiation Units and Measurements (Bethesda, MD).

**Publishing Agreement**

*It is the policy of the University to encourage the distribution of all theses, dissertations, and manuscripts. Copies of all UCSF theses, dissertations, and manuscripts will be routed to the library via the Graduate Division. The library will make all theses, dissertations, and manuscripts accessible to the public and will preserve these to the best of their abilities, in perpetuity.*

***Please sign the following statement:***

*I hereby grant permission to the Graduate Division of the University of California, San Francisco to release copies of my thesis, dissertation, or manuscript to the Campus Library to provide access and preservation, in whole or in part, in perpetuity.*

Author Signature

8/27/18
Date